Modeling Optical Properties of Non-Cubical Sea-Salt Particles

N.B. When citing this work, cite the original published paper.

(article starts on next page)

Key Points:
- The depolarization and lidar ratio of dried sea-salt aerosol are well represented by cuboidal superellipsoids over a representative size range
- Convex polyhedra provide a randomization model suitable for simulating random model errors
- Model geometries strongly deviating from cubes, such as octahedra and Gaussian random cubes, overestimate the depolarization ratio

Author Contributions:
Conceptualization: Franz Kanngießer, Michael Kahnert
Funding acquisition: Michael Kahnert
Investigation: Franz Kanngießer, Michael Kahnert
Methodology: Franz Kanngießer, Michael Kahnert
Project Administration: Franz Kanngießer, Michael Kahnert
Software: Franz Kanngießer, Michael Kahnert
Supervision: Michael Kahnert
Writing – review & editing: Franz Kanngießer, Michael Kahnert
Writing – Original Draft Preparation: Franz Kanngießer

Modeling Optical Properties of Non-Cubical Sea-Salt Particles

Franz Kanngießer[1] and **Michael Kahnert[1,2]**

[1]Department of Space, Earth and Environment, Chalmers University of Technology, Gothenburg, Sweden, [2]Research Department, Swedish Meteorological and Hydrological Institute, Norrköping, Sweden

Abstract Dry sodium chloride forms cubic crystals, while marine aerosol particles often display more or less irregular deviations from this ideal form. In this study, three non-ideal cuboidal and octahedral model geometries are investigated. Superellipsoids are tested as a model to simulate the linear backscatter depolarization ratio and the extinction-to-backscatter ratio. Gaussian random cubes as well as convex polyhedra are investigated as possible model candidates to quantify the error introduced by simplified model geometries, such as superellipsoids. Uncertainties in the real and imaginary part of the refractive index are studied, and their effect on the optical properties is compared to that caused by morphological variations. Optical calculations were performed at a wavelength of 532 nm using the discrete dipole approximation and the T-matrix method. The considered size range is representative for marine aerosol generated at low to moderate wind speeds. It is found that cuboidal superellipsoids predict depolarization and extinction-to-backscatter ratios that are consistent with observations. On the other hand, octahedral superellipsoids strongly overestimate the depolarization ratio. Gaussian random surface perturbations result in a positive shift of the depolarization ratio compared to cuboidal superellipsoids. By contrast, convex polyhedra yield results that more or less randomly scatter about those of regular cubes. Thus, convex polyhedra are a promising candidate for modeling random errors, while Gaussian random cubes are not. Uncertainties in the refractive index result in perturbations of the depolarization and extinction-to-backscatter ratio that are of comparable magnitude as those caused by perturbations of the geometry.

1. Introduction

Marine aerosol is one of the most abundant aerosol types in the atmosphere (Boucher, 2015). It consists mainly of more or less hydrated sea-salt particles as well as biological material (Boucher, 2015; Patterson et al., 2016; Zieger et al., 2017). The aerosol is emitted into the atmosphere by bursting air bubbles in the oceans and by wind tearing off wave crests (Boucher, 2015). Sea water (e.g., Wells, 2011) contains a mixture of different salts in solution, which is dominated by sodium chloride (NaCl) (Chi et al., 2015; Irshad et al., 2009; King et al., 2012; Pósfai et al., 1995; Tang et al., 1997; Ueda et al., 2014).

Marine aerosol provides large surface areas for heterogeneous chemical reactions. It further influences the climate both directly and indirectly, namely, by directly scattering radiation (Buseck & Pósfai, 1999; King et al., 2012; Murphy et al., 1998), and by acting as cloud condensation nuclei, hence impacting cloud reflectivity and precipitation (Boucher, 2015). Furthermore, sea-salt aerosol plays an important role in corrosion processes of metals and reinforced concrete structures in coastal areas (Meira et al., 2008).

Large-scale transport models typically contain sea-salt modules that describe the generation, hydration or dehydration, transport, and deposition of marine aerosol (e.g., Foltescu et al., 2005). Evaluation of such models requires the use of long-term data sets with global coverage, which can be obtained from remote sensing observations. The analyses of remote sensing observations, in turn, require a thorough understanding of the connection between aerosol microphysical properties and optical properties.

Especially in the tropics crystalline sea-salt aerosol can play significant role. The tropical troposphere is commonly characterized by the trade wind inversion, which has a lower boundary within the lowest 2 km. The trade wind inversion does not necessarily coincide with the top of the atmospheric boundary layer, as discussed by Carrillo et al. (2016) and references therein. Within this inversion layer, the moisture content rapidly decreases, so that the troposphere above that inversion layer is extremely dry (Krishnamurti et al., 2013). Aerosol lifted into or above the inversion layer dries out; as a consequence, sea-salt aerosol

Table 1

Depolarization Ratios δ_l and Extinction-to-Backscatter Ratios S_p of Dried Sea-Salt Aerosol Particles From Lidar Measurements at 532 nm and the Corresponding Relative Humidity (RH) of the Aerosol Layer

Location	δ_l (%)	S_p (sr)	RH	Reference
Husbands, Barbados	14.8 ± 3.5	25 ± 3	40%	Haarig et al. (2017)
Atlantic Ocean (near Cape Town)	9	13 ± 3	<40% (50%)	Bohlmann et al. (2018)
Atlantic Ocean (west of Western Sahara)	8	–	~10%	Yin et al. (2019)
Tokyo, Japan	10	–	<50%	Murayama et al. (1999)
Hagoya, Japan	10–20	–	25%–45%	Sakai et al. (2000)

particles may crystallize as proposed by Haarig et al. (2017). But even measurements performed in extra-tropical latitudes indicate the potential presence of dried sea-salt aerosol (Sakai et al., 2000).

Dried sea-salt particles come in cubical or cuboidal shapes, or in shapes deviating slightly from such a reference shape, as images of particle samples indicate (Gwaze et al., 2007; King et al., 2012; McInnes et al., 1994; Patterson et al., 2016; Peart & Evans, 2011; Zeng et al., 2013). Measurements of the dynamic shape factor of artificial sea salt, reported by Zieger et al. (2017), indicate aspherical, cube-like shapes. Less common are irregular shapes, which were reported by Sakai et al. (2010); Peart and Evans (2011); Zeng et al. (2013). The shape of salt crystals differs for different salts (Pósfai et al., 1995; Wise et al., 2005). In case of mixtures, such as sea salt, already small amounts of non-NaCl components can alter the shape of the sea-salt aerosol particles compared to pure NaCl crystals (Zieger et al., 2017). Thus, the chemical composition of sea-salt aerosol particles influences both the particle shape and the dielectrical properties, both of which impact the optical properties.

The optical properties, and more specifically the linear depolarization ratio of sea-salt aerosol particles have previously been measured in laboratory studies and during lidar field observations. Lab measurements of the linear depolarization ratio in the near-backscattering direction of pure NaCl crystals yielded values of $\delta_{l,179°} = 21\%$ at 532 nm wavelength (Sakai et al., 2010), and $\delta_{l,178°} \approx 25\%$ at 488 nm (Järvinen et al., 2016). For crystalline sea salt at 532 nm, a value of $\delta_{l,179°} = 8\%$ was reported (Sakai et al., 2010). Further, the depolarization ratio is dependent on the relative humidity (RH) of the ambient air. At 632.8 nm values of δ_l ranging from 5.6%–11.1% for $77\% < RH < 92\%$ and $\delta_l \approx 20\%$ for $RH < 12\%$ for NaCl particles in a lab environment have been reported in the near-backscattering direction, that is, $\vartheta > 177°$ (Cooper et al., 1974).

While there are various lidar field observations of marine or sea-salt aerosol, there are only a limited number of reported measurements of the linear depolarization ratio in combination with reported values of the relative humidity. The combination of measuring the linear depolarization ratio of marine aerosol particles and the relative humidity in the same layer can indicate the presence of dried sea-salt aerosol particles. In Table 1, values of linear depolarization ratio δ_l and extinction-to-backscatter ratio S_p at 532 nm obtained from lidar field measurements of dried marine aerosol are shown. The classification as marine aerosol is taken from each reference and usually based on backward trajectory analyses.

Sea-salt aerosol particles grow with increasing relative humidity by water vapor condensing onto the crystal (Shettle & Fenn, 1979). The crystal gets increasingly dissolved by the condensed water. If the deliquescence point, which for sea-salt crystals is at a relative humidity of approximately 70%–74% (Tang et al., 1997; Zieger et al., 2017), is reached, the salt crystal becomes fully dissolved in a liquid droplet. A liquid droplet containing dissolved sea salt remains liquid until the relative humidity is below 45%–50% (Tang et al., 1997; Zieger et al., 2017), at which point the salt recrystallizes. Between values of the relative humidity of ~50 and ~70% both crystalline, aspherical and dissolved, spherical sea-salt aerosol particles may coexist as a consequence of this hysteresis effect. Therefore, aerosol layers with reported values of relative humidity below 50% (Zieger et al., 2017) are considered to be dried and hence crystalline.

The values reported by Sakai et al. (2000) should be taken with a grain of salt, as they can be partially contaminated by continental aerosol particles. For the measurements conducted on the Atlantic Ocean near Cape Town (Bohlmann et al., 2018), two values of RH were reported. The value of $RH \approx 50\%$ was obtained by a radiosonde and the value of $RH < 40\%$ was taken from the Global Data Assimilation System (GDAS1).

Values of δ_l up to 11% for marine aerosol as reported by Groß et al. (2013) indicate the presence of dried sea-salt particles, however, the lack of reported RH measurements makes it difficult to assess this. For a relative humidity of $RH > 80\%$ values of the linear depolarization ratio of 6%–7% were reported by Sakai et al. (2012). Based on these field observations as well as the laboratory experiments, linear depolarization ratios of up to 20%–25% and extinction-to-scatter ratios of up to 25 sr particles can be considered plausible for dried (sea) salt aerosol.

The values of the near-backscattering linear depolarization ratio for pure, crystalline NaCl reported from laboratory measurements by Cooper et al. (1974); Sakai et al. (2010); Järvinen et al. (2016) (note that the measurements by Cooper et al. (1974); Järvinen et al. (2016) were not performed at $\lambda = 532$ nm) are larger than the depolarization ratio for crystalline sea salt, as reported from both laboratory measurements (Sakai et al., 2010) and from most lidar field observations listed in Table 1. The images of the salt particles, analyzed by Sakai et al. (2010), indicate that sea-salt particles have an irregular, non-cubical shape, whereas pure NaCl particles have regular geometries with sharper edges. The laboratory measurements for pure NaCl with a mode radius of $r = 0.12$ μm could be reproduced using cubes with an effective radius of $r_{eff} = 0.5$ μm (Sakai et al., 2010). By modeling size averaged linear depolarization ratio, it was found, that cubes, following the same size distribution as the measurements, underestimate the measured depolarization ratio (Bi, Lin, Wang, et al., 2018) by about a factor of 2.

Compared to mineral dust and soot aerosol (see e.g., the studies by Nousiainen and Kandler (2015); Kahnert and KanngieSSer (2020) and references therein) the approaches to modeling optical properties of sea-salt particles are less studied. Sea-salt aerosol particles have been modeled by using spheres (Chamaillard et al., 2006) and cubes (Chamaillard et al., 2006; David et al., 2013; Haarig et al., 2017; Murayama et al., 1999; Sakai et al., 2010). Spheres, cubes, and elongated and flattened cuboids are used by Adachi and Buseck (2015) as model particles to assess effects on light scattering. In order to model depolarization ratios, cubes were used by David et al. (2013); Haarig et al. (2017); Murayama et al. (1999); Sakai et al. (2010). Bi, Lin, Wang, et al. (2018) demonstrated the applicability of superellipsoids to model the depolarization of sea-salt aerosol particles. In that study, superellipsoids resembling rounded cubes, spheres, and rounded octahedra as well as distortions of these base solids by changing the aspect ratio were considered. Sea-salt aerosol with a water coating was investigated in regard to the depolarization ratio (Bi, Lin, Wang, et al., 2018), and in regard to the impact on radiative forcing (Wang et al., 2019).

For large-scale applications, such as inversion of global remote sensing observations, or assimilation of such observations into regional and global chemical transport models, one needs to employ simple and robust aerosol-optics models. In addition, one needs to quantitatively understand the error introduced by employing such a simple model. This error estimate enters into the observation error covariance matrix, which is an essential ingredient in inverse methods. Following the definition given by Kahnert et al. (2020), a simple model particle has to fulfill some or all of the following properties.

1. The model simplifies the morphology as much as possible;
2. It has only a small number of free tuning parameters;
3. It covers a large range of values of the optical parameters by varying the tuning parameters; and
4. It simultaneously reproduces several of the optical properties for a range of particle sizes, wavelengths, and compositions

We know that superellipsoids do fulfill at least properties 1–3 (Bi, Lin, Wang, et al., 2018). We will, therefore, use this geometry as a reference. However, studies on mineral dust have taught us that particles that fulfill property 3 for any given optical property have a tendency to grossly overestimate the model error for that optical property (Kahnert et al., 2020). By contrast, it was found that irregular particle models based on random distortions of the simple reference geometry can provide realistic estimates of the model error variances, provided that one employs a sufficiently large ensemble of random geometries (Kahnert et al., 2020). Experience with modeling polarimetric properties of mineral dust has also taught us that uncertainties in the refractive index can be significant. Since variations in the refractive index are difficult to account for in large-scale applications, this source of uncertainty is usually included in the estimate of the model error (e.g., Kahnert et al., 2020).

Based on lessons learned from mineral dust, we will investigate the following questions for sea salt.
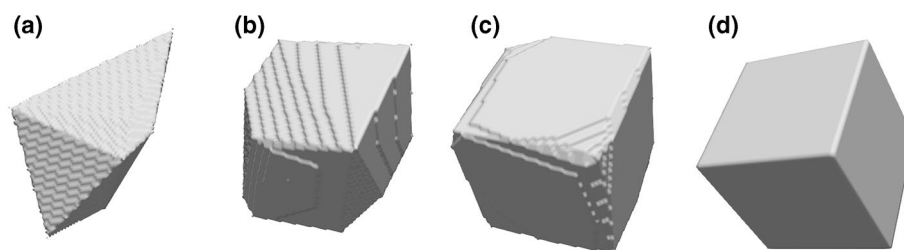
Figure 1. Convex polyhedra with different number of points included in the convex hull N (a–c) and a cube for comparison (d). The number of points increases from left to right: $N_c = 10$ (a), $N_c = 100$ (b), and $N_c = 1,000$ (c). The cube (d) corresponds to $N_c \rightarrow \infty$.

- We know that superellipsoids can be tuned to reproduce depolarization by sea salt. What are the prospects of generalizing this to simultaneously mimic depolarization and the lidar ratio of sea-salt particles?
- Are random distortions of a cubic reference shape a viable approach for estimating error variances in optics models based on the use of cubic or cuboidal model particles? Are there differences between different randomization approaches?
- The variable composition of sea salt results in a variation in the refractive index, which affects the optical properties. How large is the impact of this source of uncertainty compared to that of the variation in the geometry?

The focus in this investigation will be on the linear depolarization ratio and on the extinction-to-backscatter ratio (or lidar ratio).

2. Particle Geometries

We use superellipsoids as a reference shape, in which we vary the roundness of the edges. Both cubical and octahedral superellipsoids will be considered. Further, we investigate two approaches for considering irregular randomizations of a cubical reference shape, namely, by using convex polyhedra and Gaussian random cubes.

2.1. Convex Polyhedra

Based on irregularly shaped dust model particles used for radiative forcing calculations by Torge et al. (2011), convex polyhedra were created. N_c points were randomly placed in a Cartesian coordinate system, and around these points a convex hull is placed. This results in an irregular shape with a surface composed of plane faces. The convex hull is constructed using the quickhull algorithm (Barber et al., 1996) as implemented in the SciPy library for Python (Virtanen et al., 2020). As the points are randomly placed in a Cartesian coordinate system the shape of the convex polyhedron converges to a cubical shape for a sufficiently large number of points N_c. Here, $N_c = 10$, $N_c = 100$, and $N_c = 1,000$ were used. For each value of N_c, five different particle realizations were constructed to capture the variability associated with the random placement of the N_c points, when creating the convex polyhedra. Strictly speaking shapes like cubes or octahedra are convex polyhedra, too. For brevity, we use the term "convex polyhedra" to refer to the irregular convex polyhedra, which are neither cubical, nor octahedral.

Figure 1 shows examples for scattering geometries used in the optical calculations of such convex polyhedra with a different number of points inside the convex hull. The number of points inside the convex hulls are 10 (Figure 1a), 100 (Figure 1b), and 1,000 (Figure 1c). With growing number of points the shape increasingly resembles a cube. For comparison Figure 1d shows a cube, which corresponds to $N_c \rightarrow \infty$. The example shapes were created assuming volume discretization.

2.2. Gaussian Random Cubes

By Gaussian random cubes we refer to shapes obtained by superimposing Gaussian random perturbations onto a cube using a modified version of the G-sphere algorithm (Muinonen et al., 1996). The Gaussian
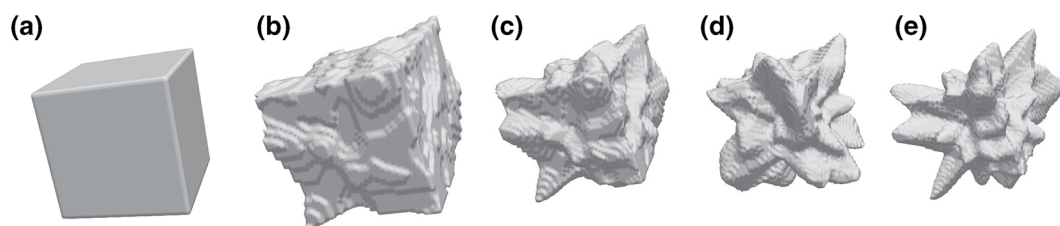
Figure 2. Example of Gaussian random cubes with $\Gamma = 10°$ and increasing radial standard deviation σ_r. (b) $\sigma_r = 0.05$, (c) $\sigma_r = 0.1$, (d) $\sigma_r = 0.15$, and (e) $\sigma_r = 0.2$ compared to a cube (a).

random perturbations are described by two different parameters, the relative radial standard deviation σ_r, which determines the magnitude of the perturbations, and the correlation angle Γ, which determines the angular scale of the fluctuations. The smaller Γ, the higher the angular frequency of the random surface perturbations (Muinonen et al., 1996). More specifically, given a surface parameterization $r_{cube}(\theta, \phi)$ of the surface of a cube in spherical coordinates, and given the surface parameterization $r_{GRS}(\sigma_r, \Gamma; \theta, \phi)$ of a unit Gaussian random sphere with radial relative standard deviation σ_r and correlation angle Γ (Muinonen et al., 1996), we define the surface parameterization $r(\theta, \phi)$ of the Gaussian random cube by

$$r(\theta,\phi) = r_{cube}(\theta,\phi) \cdot r_{GRS}(\sigma_r,\Gamma;\theta,\phi). \tag{1}$$

For the radial standard deviation of the perturbations we chose $\sigma_r = 0.05, 0.1, 0.15, 0.2$, and for the correlation angle $\Gamma = 10°, 20°, 30°$, and $90°$. For each of the configurations five different stochastic realizations were created to capture the variation due to the random nature of the perturbations. The chosen values were based on the theoretical study on Gaussian random spheres by Muinonen et al. (1996).

Figure 2 shows Gaussian random cubes with a fixed correlation angle $\Gamma = 10°$ (b–e) and a cube (a) for comparison. As for Figure 1 volume discretization was used for depicting these shapes. The relative standard deviation of the radius increases by steps of $\Delta\sigma_r = 0.05$ from $\sigma_r = 0.05$ (b) to $\sigma_r = 0.2$ (e).

Comparing with reported images of dried sea-salt aerosol (Gwaze et al., 2007; King et al., 2012; McInnes et al., 1994; Patterson et al., 2016; Peart & Evans, 2011; Sakai et al., 2010; Zeng et al., 2013) radial standard deviations of $\sigma_r > 0.1$ appear not to be representative of typical atmospheric and laboratory samples. Nevertheless, we include these values here to study the effect of more extreme deviations from cubical shape.

Figure 3 is analogous to Figure 2, but showing different values of the correlation angle Γ at a fixed radial standard deviation $\sigma_r = 0.1$ (b–e). The correlation angles increase from left ($\Gamma = 10°$, (b)) to right ($\Gamma = 90°$, (e)).

2.3. Superellipsoids

Superellipsoids are three-dimensional shapes represented by the product of super-quadratic curves and can be considered generalizations of ellipsoids (Barr, 1981; Wriedt, 2002). The suitability of superellipsoids for modeling depolarization ratios of mineral dust (Bi, Lin, Liu, et al., 2018) and sea-salt aerosol (Bi, Lin, Wang, et al., 2018) were previously demonstrated. In those studies, the invariant embedding T-matrix method has been employed (Bi et al., 2013; Johnson, 1988; Sun et al., 2019). Various different solids ranging from cuboids, cylinders, spheres to octahedra can be obtained as realizations of superellipsoids (e.g., see
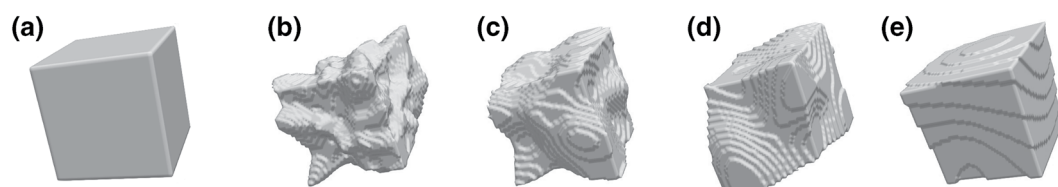

Figure 3. Example of Gaussian random cube with $\sigma_r = 0.1$ and increasing correlation angle Γ. (b) $\Gamma = 10°$, (c) $\Gamma = 20°$, (d) $\Gamma = 30°$, and (e) $\Gamma = 90°$ compared to a cube (a).
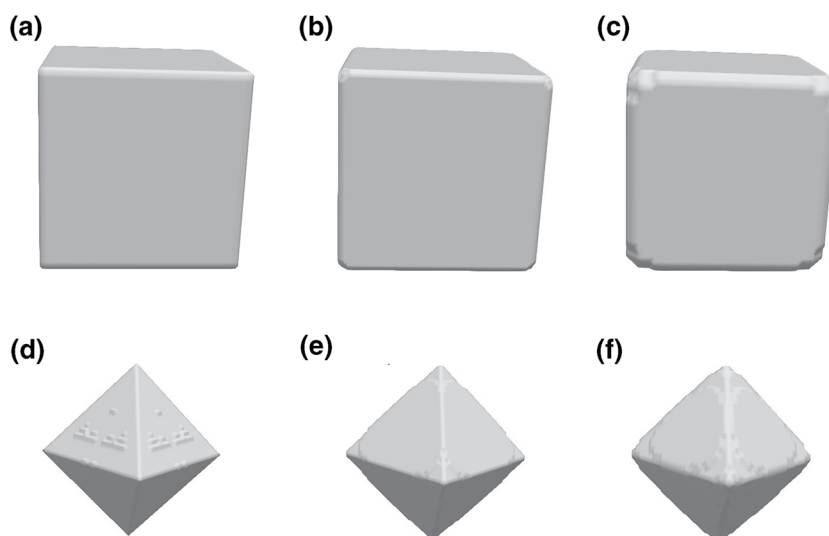
Figure 4. Examples of cube-like superellipsoids (top row) and octahedron-like superellipsoids (bottom row). The roundness increases from left to right. (a and d) Show sharp-edged geometries with $n = 0$ and $n = 2$, respectively. (b and e) Show geometries with $n = 0.1$ and $n = 1.9$, respectively. (c and f) Show geometries with $n = 0.2$ and $n = 1.8$, respectively.

Wriedt (2002)). The superellipsoidal equation for a Cartesian coordinate system with coordinates x, y, and z is (Barr, 1981; Wriedt, 2002)

$$\left[\left(\frac{x}{a} \right)^{\frac{2}{e}} + \left(\frac{y}{b} \right)^{\frac{2}{e}} \right]^{\frac{e}{n}} + \left(\frac{z}{c} \right)^{\frac{2}{n}} = 1 \tag{2}$$

The particle's extent along the three Cartesian axes x, y, and z is determined by a, b, and c, respectively. n and e are the roundness parameters in north-south (or polar) and east-west (or azimuthal) direction, respectively, which specify the shape. Variation of n and e allows for flexible modeling of a particle's roundness. Here we follow the approach by Bi, Lin, Liu, et al. (2018); Bi, Lin, Wang, et al. (2018) by assuming $a = b$ and $n = e$.

To investigate the impact of sharp edges we consider a cube (corresponding to $n = 0$) and slightly rounded cubes ($n = 0.1$ and $n = 0.2$), as well as an octahedron ($n = 2.0$) and rounded octahedra ($n = 1.9$ and $n = 1.8$). A spheroid would have a roundness parameter of $n = e = 1$. The aspect ratio was assumed to be 1, that is, $a = c$. The superellipsoids used for optical modeling are shown in Figure 4. The cube and the rounded cubes are shown in the top row (a–c) and the octahedron and the rounded octahedra are shown in the bottom row (d–f). In both rows, the roundness increases from left to right. The sharp-edged shapes are in the left column (a and d), the middle column (b and e) and the right column (c and f) show shapes with slightly rounded shapes. As these images display the input scatterers for the optical calculation volume discretization was used for depiction.

2.4. Size Distribution of Marine Aerosol

We start by investigating optical properties for randomly oriented particles of a definite size. The focus on monodisperse particles has advantages both for the analysis of results as well as for the practical implementation of the investigation. Subtle differences in optical properties due to morphological variations are more apparent when comparing monodisperse particles. Size averaging can blur out these differences, thus making it more difficult to understand the relation between morphological and optical properties. From a practical point of view, size-averaging typically requires computations for a large number of discrete sizes, which is often computationally unfeasible for irregularly shaped particles. Thus, when focusing on a

few definite sizes we can often afford to consider morphologically highly complex particles. On the other hand, size distributions of aerosols are more realistic; but the high computational requirements limit us to using fast computational methods, which are often tailored to particles with geometric symmetries (e.g., Kahnert, 2013a, 2013b). Here, we limit our investigation of size-averaged optical properties to cube-like superellipsoids with $e = n = 0, 0.1,$ and 0.2. For these geometries, we can employ the T-matrix method which is faster than the DDA, by several orders of magnitude. For example, computing the optical properties for superellipsoids with $r_{ve} = 1.0$ μm and $n = 1.8$ using the DDA with the specifications given below, required 8,395 core hours, corresponding to the equivalent of more than 11.5 months of calculations on a single core. The corresponding T-matrix computations took less than 2 min. The DDA calculations for a superellipsoid with $r_{ve} = 1.0$ μm and $n = 2.0$, required 10,763 core hours, corresponding to nearly 1.25 years of calculations on a single core. The corresponding T-matrix results had to be averaged over seven different values of the cut-off parameter, which required a total of 8.5 min of computation time. Note, however, that in this study smaller volume elements than the ADDA default size were used, which contributed to the high computational demand of the DDA calculations. (The reasoning for this choice is explained in Section 3). Also, the symmetries of superellipsoids have not been exploited in setting the range of orientational angles. Doing so could save about a factor of 16 in the time required for the DDA computations.

This illustrates that it is hardly feasible to compute DDA results averaged over a large number of particle sizes. The high computational speed of the T-matrix method derives from two features, namely, (i) orientation-averaging is done analytically, and (ii) the Tsym code exploits particle symmetries by making use of commutation relations of the T-matrix as well as irreducible representations of the pertinent symmetry group (Kahnert, 2013a).

For the size averaging of superellipsoids, we use two different types of size distributions.

1. We consider a monomodal log-normal size distribution

$$n_{\text{mono}}(r_{ve}; N, r_0, \sigma_n) = \frac{N}{r_{ve} \ln \sigma_n \sqrt{2\pi}} \exp\left[-\frac{\ln^2(r_{ve} \, / \, r_0)}{2 \ln^2 \sigma_n} \right],$$ (3)

where, N is the particle number density, n_{mono} describes the number of particles per volume element per size interval, r_{ve} is the volume-equivalent radius of the particles, r_0 is the median radius, and σ_n represents the geometric standard deviation. In our calculations we use $\sigma_n = 1.5$ and $r_0 = 0.1, 0.2, ..., 1.5$ μm. Size averaging of the optical properties involves integration of the scattering matrix elements, weighted by the scattering cross section and the size distribution. Numerically, we perform the integration by use of 146 equally spaced particle sizes 0.050, 0.067, ..., 2.509 μm.

2. Marine aerosol is often best described by a bimodal size distribution. Thus, as a more realistic case, we consider a bimodal log-normal size distribution given by

$$n_{\text{bimodal}}(r_{ve}; N_1, r_{0,1}, \sigma_{n,1}, N_2, r_{0,2}, \sigma_{n,2}) = \\ n_{\text{mono}}(r_{ve}; N_1, r_{0,1}, \sigma_{n,1}) + n_{\text{mono}}(r_{ve}; N_2, r_{0,2}, \sigma_{n,2}).$$ (4)

For the median radii, geometric standard deviations, and number densities in each mode we use 12 different combinations of parameters taken from the study by Porter and Clarke (1997) (to be more specific Table 2 therein). They are based on observations in the marine boundary layer at winds speed varying between 0.4 to more than 33 m/s. Note, however, that marine aerosol populations at high wind speeds would contain considerable number densities of coarse aerosol. We are limited by computational constraints to particles radii not exceeding 2.509 μm. Thus our computation cannot be regarded as covering a similar range of wind speeds as the size distributions given by Porter and Clarke (1997).

For either size distribution, we present the size-averaged optical properties as functions of the effective radius

$$r_{\text{eff}} = \frac{\int_0^\infty n_{\text{m/b}}(r_{ve}) r_{ve} \pi r_{ve}^2 \mathrm{d}r_{ve}}{\int_0^\infty n_{\text{m/b}}(r_{ve}) \pi r_{ve}^2 \mathrm{d}r_{ve}},$$ (5)

where $n_{m/b}$ denotes either the monomodal or the bimodal log-normal size distribution. Thus the effective radius represents the ratio of the third and the second moment of the size distribution. It is a quantity frequently employed for characterizing the size of polydisperse particles in light-scattering processes (e.g., Mishchenko et al., 2002).

3. Optical Modeling

The optical calculations were performed for a wavelength of 532 nm. This is the second harmonic of neodymium-doped yttrium aluminum garnet (Nd:YAG) lasers, which are commonly used in lidar instruments (Eloranta, 2005; Wandinger, 2005).

The refractive index of NaCl as given by Eldridge and Palik (1997) was used as a reference value in this study, as sea salt is dominated by sodium chloride. Thus we assume $m = 1.5484 + i0$. Note that the imaginary part of the refractive index is zero, that is, the particles are assumed to be non-absorbing. However, marine aerosol can contain varying amounts of organic substances and dimethyl sulfide (DMS). The presence of absorbing organic material can increase the imaginary part of the refractive index. DMS, which is optically softer than NaCl, may lower the real part of the refractive index. Further, the refractive index of sea-salt aerosol has a weak dependence on the relative humidity (Cotterell et al., 2017; Shettle & Fenn, 1979). Correspondingly, refractive indices reported for marine aerosol vary quite considerably (Sayer et al., 2012). For instance, Hänel (1976) reported slightly different values for dried marine aerosol ($m = 1.55 + i0.059$) and dried sea spray aerosol ($m = 1.55 + i0$). (Since Hänel (1976) reported values not directly at $\lambda = 0.532\ \mu m$, the values cited here were obtained from linear interpolation.) The latter value underscores that the refractive index of NaCl closely agrees with that of sea-salt aerosol.

In retrieval or assimilation methods, it would be impossible to account for the variable composition of marine aerosols. Rather, one would consider the variation in the refractive index as a source of uncertainty and include the corresponding changes in optical properties in the error estimates. Here, we will assess the impact of this source of uncertainty on the modeling results by considering two additional values of the refractive index, namely, $m = 1.55 + 0.059i$ and $m = 1.415 + 0.002i$. These values are taken from Hänel (1976) and Hess et al. (1998); Shettle and Fenn (1979), respectively. The value of $m = 1.55 + i0.059$ is taken as a proxy for marine aerosol with a relatively high amount of absorbing material. We use a value of $m = 1.415 + i0.002i$ (Hess et al., 1998; Shettle & Fenn, 1979) as a representative for more weakly scattering and slightly more absorbing marine aerosols.

The calculations were performed at three different volume-equivalent radii $r_{ve} = 0.25$, 0.5, and 1.0 µm. At $\lambda = 0.532\ \mu m$, these radii correspond to the size parameters $x = 2.95$, 5.91, and 11.81, respectively. Size parameter x and volume-equivalent radius r_{ve} are related by $x = 2\pi r_{ve}/\lambda$. This covers a large part of the typical size range for this kind of aerosol, although particles up to radii of 5 µm are not uncommon. However, the upper end of our size range is constrained by computational capabilities of light-scattering software.

Optical calculations were performed using the discrete dipole approximation (DDA) code ADDA, version 1.3 (Yurkin & Hoekstra, 2007, 2011). The DDA can treat arbitrary geometries, as the scatterer is divided into multiple, fully polarizable volume-elements called dipoles, which are much smaller than the wavelength. The dipoles interact with each other and the incident field, resulting in a set of linear equations, which are solved using standard numerical methods. As a consequence of dividing the scatterer into fully polarizable dipoles arbitrary geometries and inhomogeneous scatterers can be treated.

Setting up the dipole geometries, which serve as an input for the DDA calculations, is strongly connected to the definition of the scatterers' geometry on a discrete Cartesian coordinate system. As a consequence, the volume equivalent radii, at which the calculations were performed, correspond to the discretized shape in ADDA (i.e., r_{ve} corresponds to -eq_rad in ADDA).

We also performed T-matrix calculations on superellipsoids. We employed the Tsym code (Kahnert, 2013a), version 6.6α. This code is highly efficient for particles with discrete symmetries, such as superellipsoids, as it makes use of commutation relations (Schulz et al., 1999) and irreducible representations (Kahnert, 2005) of finite symmetry groups. Averaging over orientational angles is performed analytically. Here, we extended the Tsym version described by Kahnert (2013a) by including superellipsoids into the code. A major

difficulty is that Waterman's surface-integral equation method, on which this code is based, requires the surface parameterization as well as its partial derivatives in spherical coordinates. We are not aware of any publications that provide a parameterization of superellipsoids in spherical coordinates, certainly not in the light scattering literature. Equation 2 only provides us with an implicit equation of the particle surface in Cartesian coordinates. Equation 2 given by Wriedt (2002) provides a parameterization in another coordinate system, but not in spherical coordinates. Thus, we derived, implemented, and tested a surface parameterization of superellipsoids and their partial derivatives in the spherical coordinate basis. The details of this derivation are given in the Appendix A.

For ideal cubes, the code was run with the standard geometry setting 'FCCUBE' for face-centered cubes. All other geometries were run by use of the new geometry of superellipsoids. As this geometry is limited to roundness parameters n, $e < 2$, we approximate ideal octahedra by setting $n = e = 1.99$. In the computations the infinite-dimensional T-matrix has to be truncated at a finite cut-off index N_{cut} as explained in the description of the code (Kahnert, 2013a). (In the parameter file of Tsym, this parameter is called "nmax.") In all but one case considered here the computations were stable over a broad range of N_{cut} values. This is illustrated in Figure S1. However, for $r_{ev} = 1$ µm and $e = n = 1.99$, the computational results were only stable over a small range of N_{cut} values, and the optical properties were averaged over that range as explained in (Yurkin & Kahnert, 2013). The precise values of N_{cut} used in the computations are given in Tables S4 and S5.

The Tsym computations serve two main purposes. (i) We employ the T-matrix results for comparison with DDA computations (see below). (ii) DDA computations are prohibitively time consuming for computing optical properties for an entire size distribution. For this reason, we employ the T-matrix method for investigating size-averaged optical properties of superellipsoids (see Sec. 2.4).

The light scattering computations give out the optical cross sections and the full scattering matrix, from which other optical parameters can be calculated. For instance, the extinction-to-backscatter ratio S_p, which, in the context of lidar remote sensing, is frequently referred to as the lidar ratio, can be calculated for a distinct particle size r as (Gasteiger et al., 2011)

$$S_p(r) = (4\pi \frac{C_{ext}(r)}{C_{sca}(r)F_{11}(r)}|_{\vartheta=180°} \tag{6}$$

C_{ext} is the particle's extinction cross section, C_{sca} the particle's scattering cross section, and F_{11} denotes the phase function, which is the (11) element of the normalized Stokes scattering matrix.

The linear backscattering depolarization ratio can be calculated by (Mishchenko & Hovenier, 1995):

$$\delta_l = (\frac{F_{11} - F_{22}}{F_{11} + F_{22}}|_{\vartheta=180°}, \tag{7}$$

where, F_{22} denotes the (22) element of the normalized Stokes scattering matrix, and ϑ represents the scattering angle. The expression is evaluated in the backscattering direction ($\vartheta = 180°$).

The discrete dipole approximation is derived from the volume-integral equation of electromagnetic scattering under the assumption that the volume elements are much smaller than the wavelength of light. Thus, the dipole spacing is one of the main parameters that control the numerical accuracy of the results. To estimate the related numerical uncertainty, the dipole spacing for a superellipsoid with $r_{ve} = 0.5$ µm and $n = e = 0.2$ is varied. In the ADDA code, we express the dipole spacing as dipoles per wavelength (dpl). The larger we set the value of dpl, the finer the dipole grid.

Another measure to control the dipole spacing is $|m|kd$, with m being the complex refractive index of the scatterer, $k = 2\pi/\lambda$ the wavenumber in vacuum, and d the dipole spacing. dpl and $|m|kd$ can be converted into each other by $|m|kd = 2|m|\pi/dpl$ (Yurkin et al., 2006).

As we assume totally random orientation of each scatterer, the use of orientation averaging is required. The number of orientations, are controlled by another set of parameters, which impact the numerical accuracy of the results. Particle orientation with respect to the laboratory reference frame within ADDA is specified by the three Euler angles α, β, and γ. In order to get orientationally averaged results, ADDA provides an internal orientation averaging. The averaging is calculated over the Euler angles. Here, averaging over α

is performed by a single computation of internal fields, whereas averaging over β and γ is done by independent DDA simulations (Yurkin & Hoekstra, 2011). Owing to the use of Romberg integration within ADDA the angles are uniformly spaced, in case of β as values of $\cos\beta$. The set of integration points used for orientation averaging is defined by the minimum and maximum value and the minimum and maximum number of subdivisions $J_{\min}$ and $J_{\max}$. The total number of argument values of the Romberg integration is limited to $2^{J_{\max}} + 1$.

To estimate the impact of the dipole spacing, calculations for a superellipsoid with a roundness parameter $n = e = 0.2$ (i.e., a lightly rounded cube) and a superellipsoid with $n = e = 0.0$ (i.e., a cube) were performed with 16 different dipole spacings ranging between $dpl = 10$ and $dpl = 160$; the results were compared to T-matrix calculations. The estimation of the impact of the dipole spacing was performed with a constant number of 68,096 orientations (i.e., $J_{\max} = 6$ for the Euler angle α and $J_{\max} = 5$ for both the Euler angles β and γ). To assess the uncertainty related to the dipole spacing and to provide a further comparison of DDA and T-matrix results, the DDA calculations for different dipole spacing were extrapolated to infinitely small dipoles by using the method described by Yurkin et al. (2006). In this method a second order polynomial is fitted to the respective quantity as a function of $|m|kd$, the resulting polynomial is then extrapolated to $|m|kd = 0$, which would correspond to $dpl = \infty$, that is, infinitely small dipoles. The (11), (22), and (12) elements for such a superellipsoid with four different dipole spacings are shown in the left column of Figure 5. The rather coarse dipole spacing of $dpl = 10$ is indicated in dark blue, $dpl = 19$ is depicted by the green line, $dpl = 42$ in light-red, $dpl = 92$ in purple, and the finest dipole spacing of $dpl = 160$ is represented by the yellow line. The T-matrix results are shown by the light-blue line. The right column of Figure 5 shows the absolute deviation of the matrix elements with different dipole spacing from the matrix elements obtained from extrapolation of the DDA results.

The (11) element of the Stokes scattering matrix shows only comparatively little variation with changing dipole spacing for dipole spacings of $dpl \geq 19$. It should be noted, that $dpl = 10$ is below the ADDA default dipole spacing of $dpl = 10|m|$ (Yurkin & Hoekstra, 2011) (in this study $10|m| = 15.8$). The accuracy of the DDA results for optical cross sections with the ADDA default value is in the order of several percent (Draine & Flatau, 1994; Yurkin & Hoekstra, 2007, 2011), coarser dipole spacings further reduce the accuracy. The different lines for the F_{11} elements, with exception of the line for $dpl = 10$ are nearly indistinguishable by visual inspection. The (12) and (22) element of the Stokes scattering matrix converge toward the T-matrix results with increasing dpl. However, the variation of the DDA results with dpl is rather weak. For instance, the 12 and 22 elements for $dpl = 92$ (purple) are hardly distinguishable from $dpl = 160$ (yellow), or from the T-matrix results (light blue). With finer dipole spacing the deviations from the extrapolated matrix elements decrease. For the (11) and the (22) element, the T-matrix results deviate least from the corresponding matrix elements. For the (12) element, the deviations of the T-matrix results and the DDA results for $dpl = 160$ from the reference results are of similar magnitude. Considering the small differences between the extrapolated DDA results and the T-matrix results, both methods can be considered equivalent.

From the extrapolated matrix elements and the extrapolated extinction cross section, we calculated the extinction-to-backscatter ratio and the linear backscattering depolarization ratio. Figure 6 shows the absolute deviation from the extrapolated values of extinction-to-backscatter ratio (top) and linear backscattering depolarization ratio (bottom) for superellipsoids with both $n = e = 0.0$ (green) and $n = e = 0.2$ (blue). On the right of the vertical line we show the absolute deviation of the T-matrix results from the extrapolated DDA results. In case of the superellipsoid with $n = e = 0.0$ (i.e., the cube) the absolute differences between the extrapolated values for the DDA and the T-matrix are $\Delta S_p = 0.67$ sr and $\Delta \delta_l = 5.2 \cdot 10^{-3}$. For the superellipsoid with $n = e = 0.2$ the respective values are $\Delta S_p = 0.23$ sr and $\Delta \delta_l = 7.8 \cdot 10^{-4}$. From these small absolute differences, we conclude that DDA and T-matrix yield very similar results and can be used interchangeably.

In order to not overly increase the computational burden, we chose a dipole spacing corresponding to $|m|kd \leq 0.4$, or $dpl \geq 25$ respectively. As a consequence differences smaller than $\Delta \delta_l = 0.018$ and $\Delta S_p = 1$ sr, respectively, cannot be distinguished from artifacts due to dipole spacing.

To gauge the impact of the number of subdivisions and hence the impact of the number of orientations, we performed calculations for four different values of $J_{\max}$ with $J_{\max}(\beta) = J_{\max}(\gamma)$; for $J_{\max}(\alpha)$ we assumed $J_{\max}(\alpha) = J_{\max}(\beta) + 1$. An additional parameter is the required accuracy (Yurkin & Hoekstra, 2014). By setting
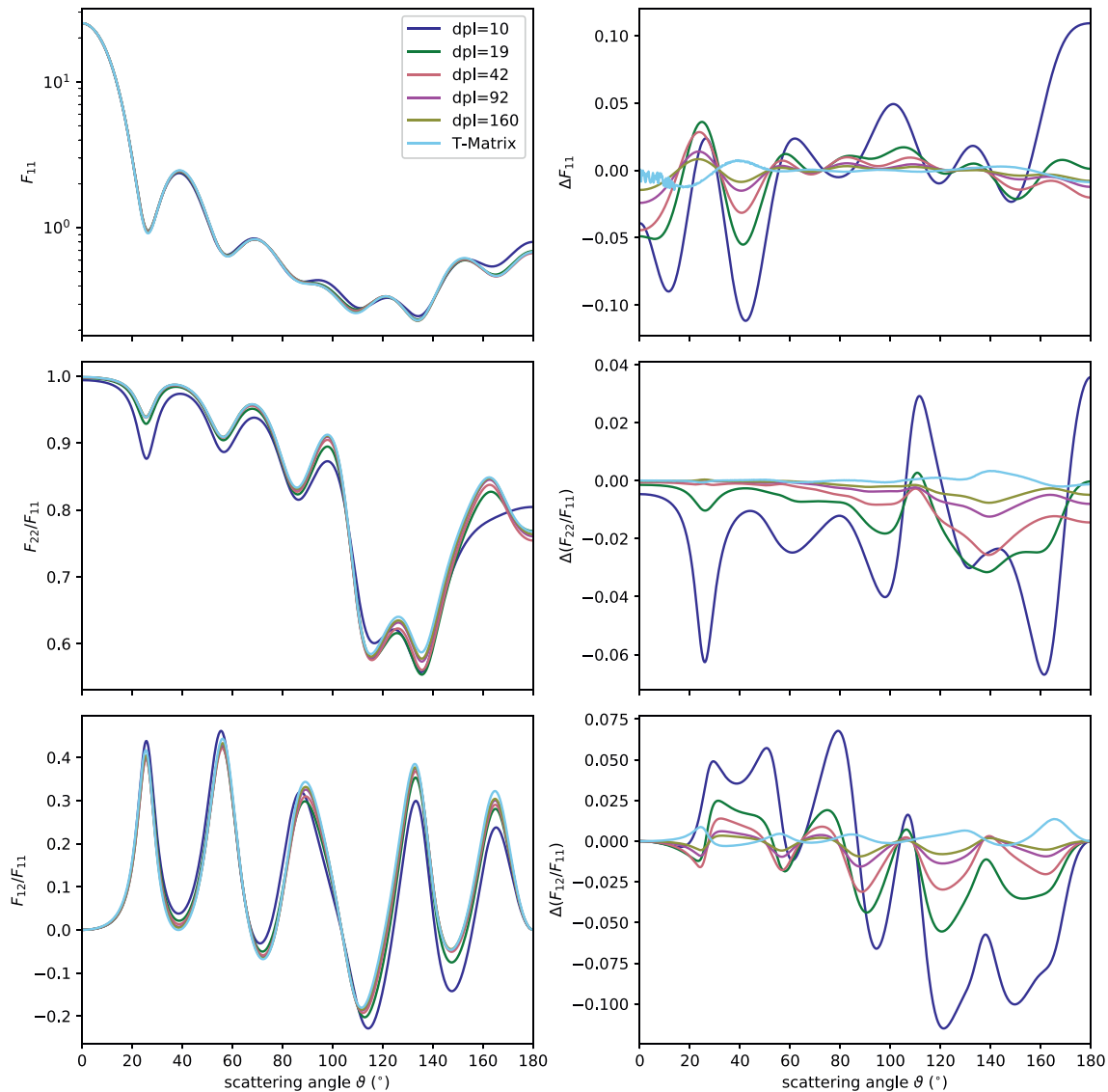
Figure 5. F_{11} (top left), F_{22}/F_{11} (middle left), and F_{12}/F_{11} (bottom left) for a superellipsoid with $n = e = 0.2$ and $r_{ve} = 0.5$ μm (see Figure 4c) and different dipole spacing, expressed as dipoles per wavelength dpl; $dpl = 10$ in dark blue, $dpl = 19$ in green, $dpl = 42$ in light-red, $dpl = 92$ in purple, and $dpl = 160$ in yellow. The light-blue line indicates the matrix elements obtained from T-matrix calculations. The right column shows the deviation of the respective matrix elements from the elements obtained by extrapolating from DDA results.

this required accuracy to zero, the calculations were performed by setting the number of subdivisions to J_{max}. The resulting F_{11}, F_{22}, and F_{12} elements of the scattering matrix are shown in Figure 7. The results for $J_{max} = 3$, resulting in 64 ADDA runs, and when considering averaging over α in 1,024 angular orientations, are shown in blue, the results for $J_{max} = 4$ (256 ADDA runs, 8,192 orientations) are shown in green, the results for $J_{max} = 5$ (1,024 ADDA runs, 68,096 orientations) in olive, and the results for $J_{max} = 6$ (4,096 ADDA runs, 524,288 orientations) in light purple. For comparison the T-matrix results are also shown in light-blue. Especially in the backscattering direction the T-matrix results are in agreement with the DDA results for $J_{max} = 6$. With exception of the F_{11} and the normalized F_{22} element in backscattering direction and the normalized F_{12} element at $\vartheta = 150°$ and $170°$ the results for $J_{max} = 5$ and $J_{max} = 6$ are indistinguishable. In backscattering direction, the relative differences of the F_{11}-element between $J_{max} = 5$ and $J_{max} = 6$ were 10.9% ($n = 0.0$) and 6.5% ($n = 0.02$). As a comparison, for irregular particles with a similar size parameter Gasteiger and Wiegner (2018) reported a relative deviation of up to 6%, although for two different numbers of orientations considered. The differences in the backscattering direction affect the backscattering
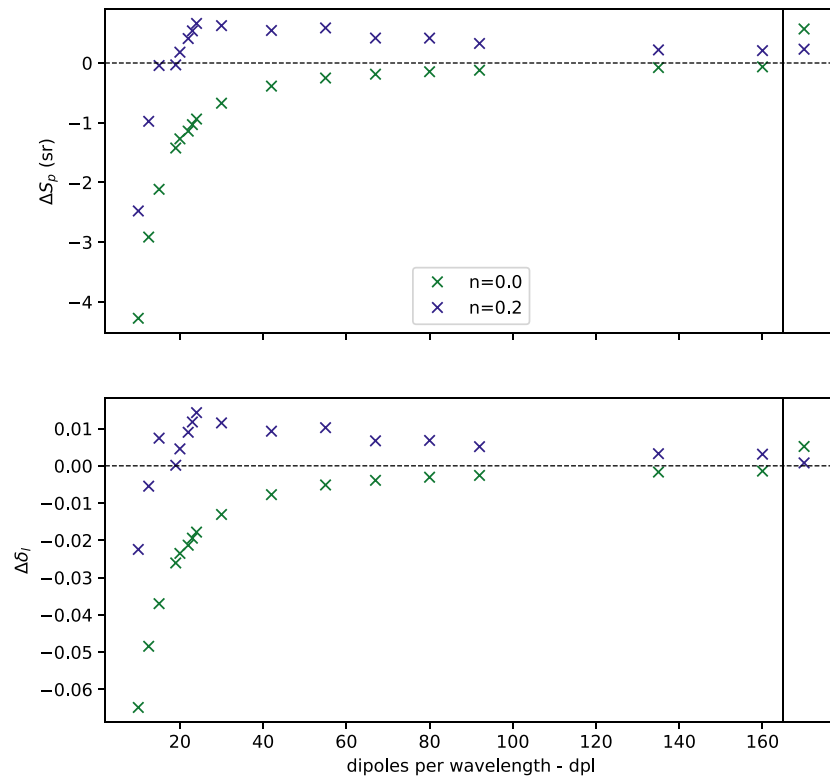
Figure 6. Absolute deviation of extinction-to-backscatter ratio (ΔS_p, top panel) and linear depolarization ratio ($\Delta \delta_l$, bottom panel) from extrapolated DDA results as a function of dipoles per wavelength (dpl). Results for a superellipsoid with $n = e = 0.0$ (i.e., a cube) are shown in green and results for a superellipsoid with $n = e = 0.2$ are shown in blue. Calculations were performed for a volume-equivalent radius of $r_{ve} = 0.5 \, \mu$m and at $\lambda = 0.532 \, \mu$m. The values right of the vertical line refer to the T-matrix results.

depolarization ratio, and the extinction-to-backscatter ratio, which are shown in Figure 8 as a function of J_{max}. The difference of δ_l between $J_{max} = 5$ and $J_{max} = 6$ is 0.015 (corresponding to 6.1%) for $n = 0.2$ and 0.022 (or 9.1%) for $n = 0.2$. In case of S_p, the corresponding differences are 1.04 sr (6.1%) and 2.06 sr (9.8%), respectively.

Analogous to the choice of dipole spacing, there is a trade-off between the accuracy of the DDA result and the number of orientations considered for orientation averaging. We chose $J_{max} = 5$ for both the Euler angles β and γ. Exploiting rotational and reflection symmetry of cubes and superellipsoids could reduce the range of the Euler angles in orientation averaging (Penttilä et al., 2007). This would reduce the computational burden of the ADDA calculations discussed in Section 2.4.

Furthermore, we used the Bi-CGStab(2) iterative solver and divided the range of the scattering angles into 720 intervals (i.e., with a resolution of 0.25°). Otherwise ADDA default settings were used.

4. Results

4.1. Convex Polyhedra

The ensemble-averaged (11), (22), and (12) elements of the normalized scattering matrix for the different convex polyhedra are shown in Figure 9. (The values shown here are tabulated in Table S1.) The rows correspond to the matrix elements and the columns to the different volume-equivalent radii. The colors indicate the results for different numbers of randomly placed points N_c, as well as for the cubes, which correspond to $N_c \rightarrow \infty$.

The values of both the convex polyhedra with $N_c = 100$ and $N_c = 1,000$ are close to the values from the cubes ($N_c \rightarrow \infty$), whereas the values for $N_c = 10$ deviate more strongly from the values for the cubes. As the
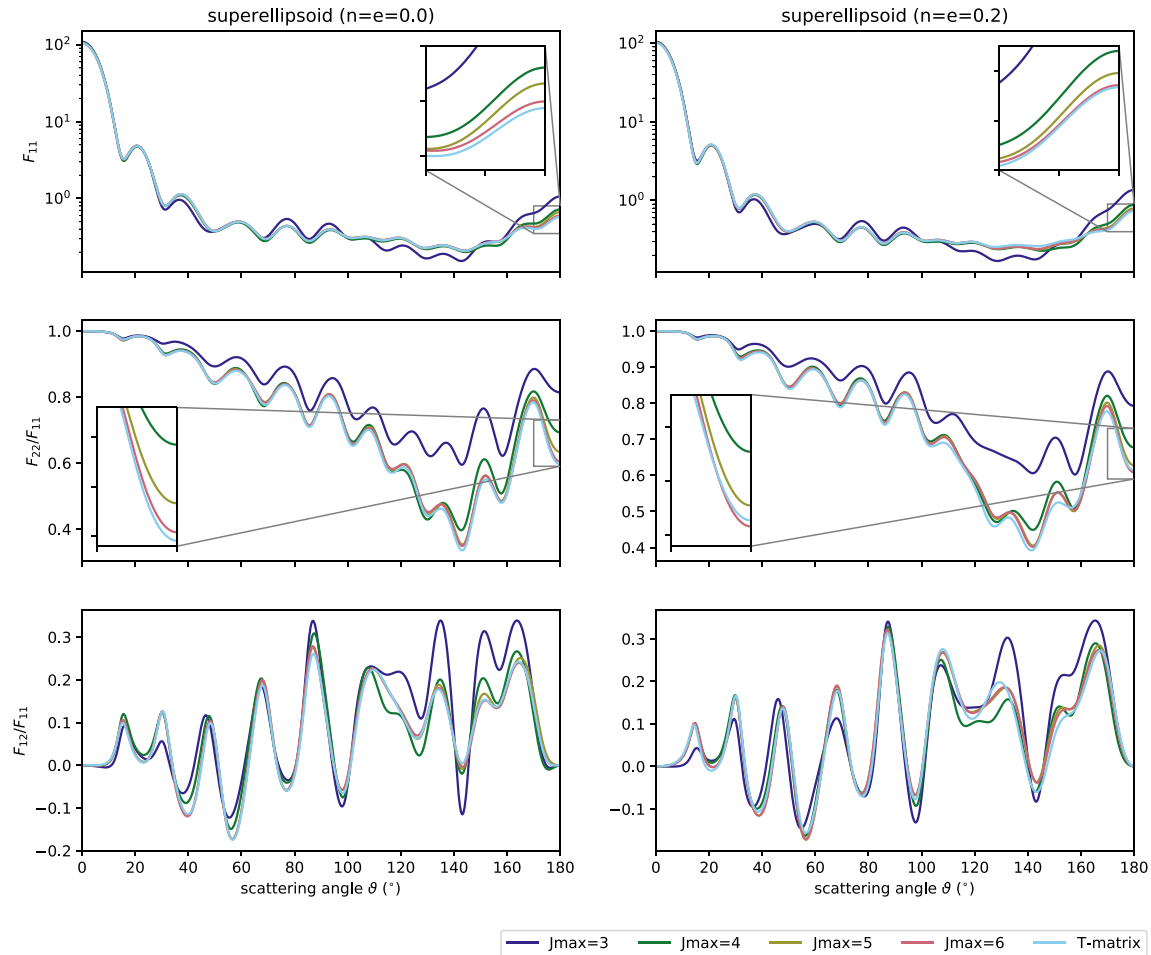
Figure 7. F_{11}, F_{12}, and F_{12} matrix elements for superellipsoids with $r_{ve} = 1.0$ μm, and $n = 0.0$ (left column) and $n = 0.2$ (right column) for different values of J_{max} (as indicated by the colors) and for T-matrix results (shown in light-blue).

example geometries shown in Figure 1 indicate, the solids with $N_c = 10$ deviate most from a cubical shape. Thus, the geometric variation closely corresponds to the variation in the scattering matrix elements.

Figure 10 shows the size-dependent backscattering cross section C_{bak}, extinction-to-backscatter ratio S_p, and linear backscattering depolarization ratio δ_l for convex polyhedra with $N_c = 10$ (dark-blue), $N_c = 100$ (green), $N_c = 1,000$ (purple), and $N \to \infty$ (cyan), which is represented by a cube. With the exception of the cube, the crosses denote the arithmetic mean over five different geometric realizations, and the bars indicate the range between the maximum and minimum of each quantity in the ensemble. To allow for an easier visual inspection the points in Figure 10, as well as in Figures 14 and 16 are slightly shifted in the x-direction. With increasing number of points, the variation in the backscattering cross section and in the extinction-to-backscatter ratio is reduced, so that for $N_c = 1,000$ the spread in the ensemble is very small. However, this does not hold for δ_l, for which the range for $N_c = 100$ with $r_{ve} > 0.5$ μm is larger than the range for $N_c = 10$. Possibly five different stochastic realizations per N_c do not sufficiently sample from the variety of possible shapes for $N_c = 10$ and hence potentially underestimate the full range of possible values.

The larger deviations in the F_{22}-element in backscattering direction for $N_c = 10$ compared to the cube ($N \to \infty$), especially for $r_{ve} = 0.5$ μm and $r_{ve} = 1.0$ μm, are mirrored in the comparatively large differences in the linear depolarization ratio. Compared to the cubical shape the convex polyhedra with $N_c = 10$ give consistently higher δ_l values. For instance, for $r_{ve} = 1$ μm, the depolarization ratio modeled with the convex particles with $N_c = 10$ is around 0.45, which is about twice as high as that obtained with $N_c \geq 100$.
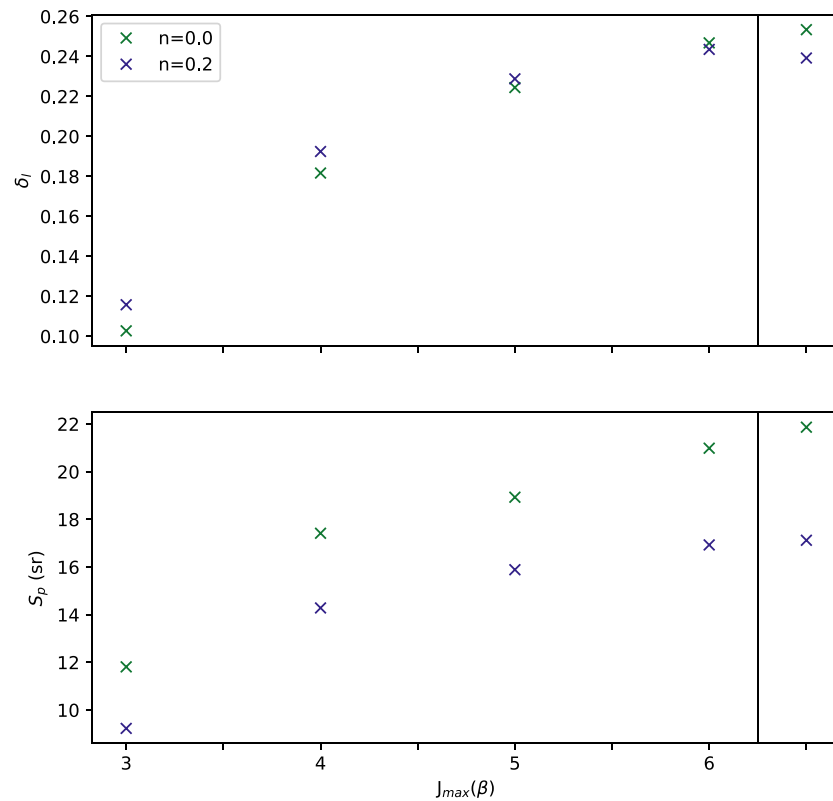
Figure 8. Linear backscattering depolarization ratio (top panel) and extinction-to-backscatter ratio (bottom panel) of superellipsoids with $r_{ve} = 1.0$ μm and $n = 0.0$ (green) and $n = 0.2$ (blue). The values right of the vertical line refer, analogously to Figure 6, to the T-matrix results.

The main general result in Figure 10 is that the convex polyhedra model yields optical properties that scatter about those obtained for cubes, provided that we exclude the rather extreme case of $N_c = 10$. This means that both positive and negative deviations from the reference results of ideal cubes are observed. As we will see in the next section, this differs markedly from the corresponding results for Gaussian random cubes. The implications of this observations will be discussed in Section 5.

4.2. Gaussian Random Cubes

As explained in Section 2.2 Gaussian random cubes are created by superimposing Gaussian distortions characterized by the correlation angle Γ and the radial standard deviation σ_r on a cube. Figures 11–13 show the (11), (22), and (12) normalized scattering matrix elements for Gaussian random cubes. Each figure shows the matrix elements for a different volume-equivalent radius (Figure 11 for $r_{ve} = 0.25$ μm, Figure 12 for $r_{ve} = 0.5$ μm, and Figure 13 for $r_{ve} = 1.0$ μm). As in Figure 9 the rows indicate the respective mean matrix elements. The columns in all three figures indicate the radial standard deviation σ_r. The left-most column shows matrix elements for $\sigma_r = 0.05$, the center-left column for $\sigma_r = 0.10$, the center-right for $\sigma_r = 0.15$, and the right-most column for $\sigma_r = 0.20$. The colors indicate the correlation angle. The results for a correlation angle of Γ = 10° are shown in dark blue, the results for Γ = 20° in green, for Γ = 30° in light red and for Γ = 90° in yellow.

For comparison, we added the corresponding matrix elements of a cube of the same volume-equivalent radius, shown in purple.

Inspection of Figures 11–13 reveals several interesting features related to the random surface perturbations. Among the more predictable phenomena is a steadily increasing deviation from the scattering matrix elements of the cube with increasing radial standard deviation σ_r (moving from left to right through the columns). Further, by comparing the three figures, we clearly see that the effect of surface perturbations
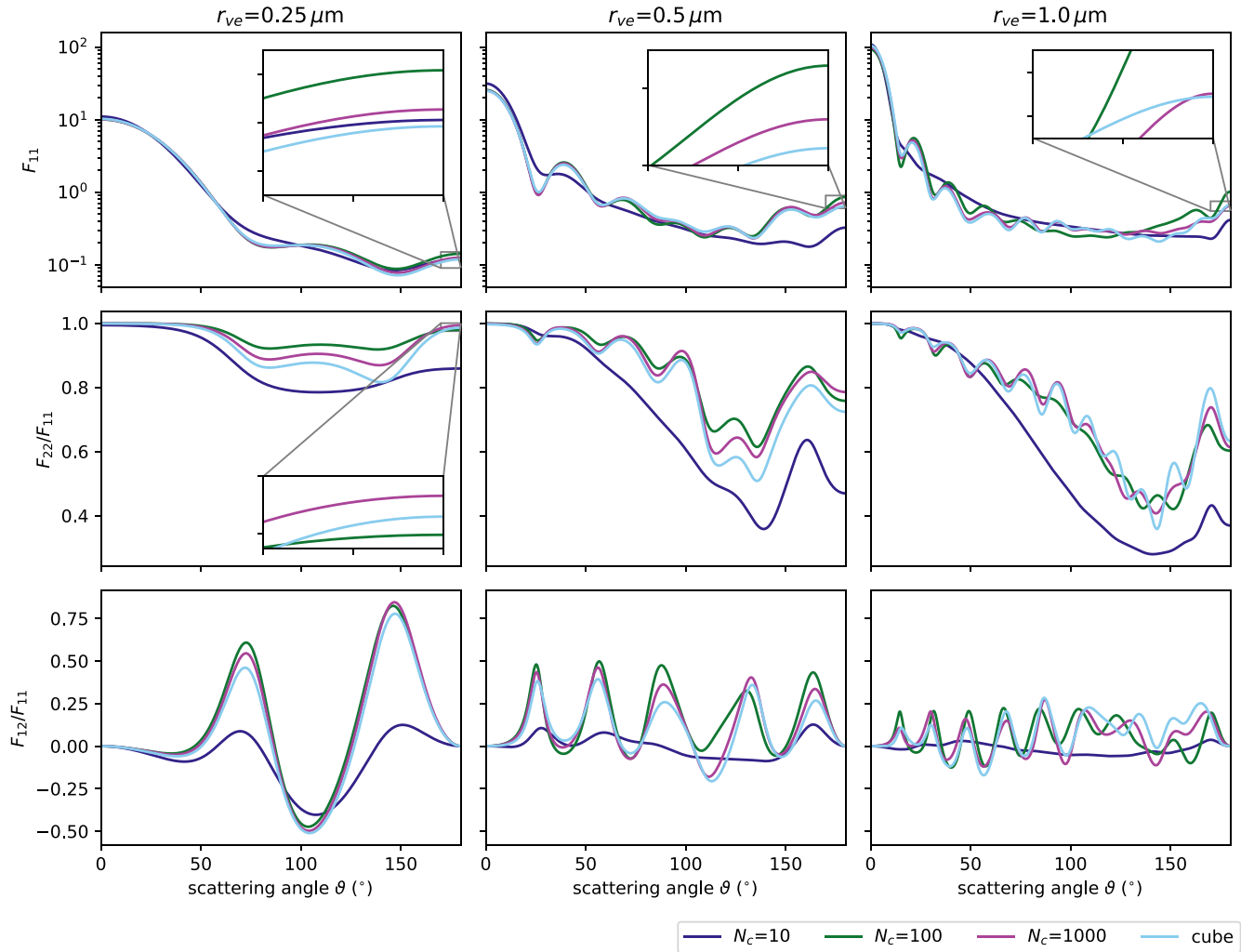
Figure 9. (11), (22), and (12) elements of the normalized scattering matrix for convex polyhedral shapes with $N_c = 10$ (dark blue), $N_c = 100$ (green), $N_c = 1,000$ (purple), and for a cube, corresponding to $N \rightarrow \infty$ (cyan). The (22) and (12) elements are normalized with respect to the (11) element. The matrix elements, with exception for the ones of the cube were averaged over five different geometrical realizations. The columns represent the three different volume-equivalent radii $r_{ve} = 0.25$ μm (left column), $r_{ve} = 0.5$ μm (center column), and $r_{ve} = 1.0$ μm (right column).

becomes more pronounced for larger particles. For the largest particles (see Figure 13) it becomes particularly apparent that the impact of the surface perturbation is most pronounced for the shortest correlations angles. For small angles Γ and high values of σ_r the Gaussian random perturbations of the reference geometry tend to smooth out some of the oscillations in the (12) and (22) elements of the scattering matrix. Finally, we see in all three figures that, overall, the surface perturbation impacts the polarization and depolarization-related scattering matrix elements F_{12} and F_{22} more dramatically than the phase function F_{11}. While the (11) and (22) elements are fairly sensitive in the backscattering direction, the (12) element is mostly perturbed at angles away from the exact forward and backward-scattering directions.

Figure 14 shows the size-dependent backscattering cross section (left column), extinction-to-backscatter ratio (center column), and the linear depolarization ratio (right column) for different correlation angles (colors as in Figures 11–13) and radial standard deviations. The different radial standard deviations are represented in the different rows. The top row corresponds to $\sigma_r = 0.05$, the second to top row $\sigma_r = 0.1$, the third $\sigma_r = 0.15$, and the the bottom row to $\sigma_r = 0.2$. The values shown in Figure 14 are also tabulated in Table S2.
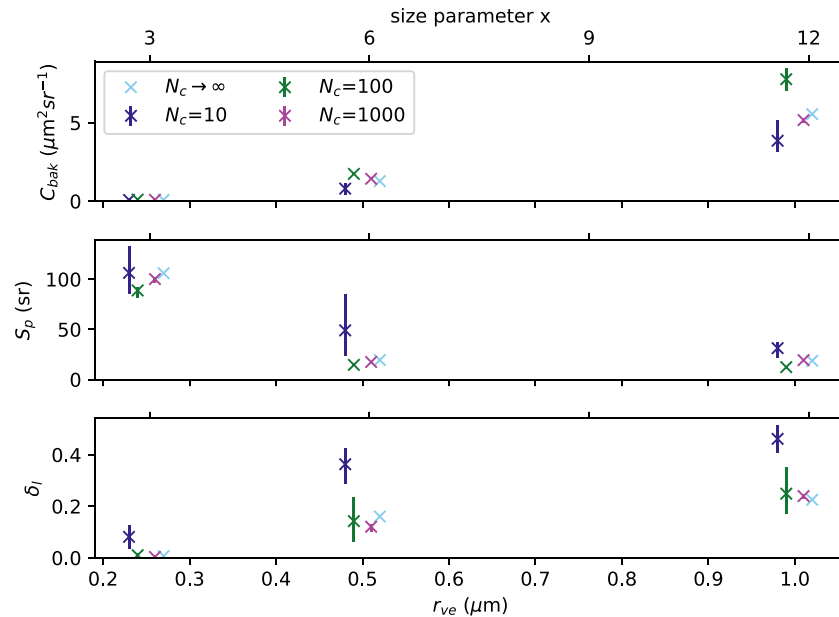
Figure 10. Size-dependent backscattering cross section C_{bak} (top row), extinction-to-backscatter ratio S_p (middle row), linear backscattering depolarization ratio δ_l (bottom row) for cubes, corresponding to $N_c \rightarrow \infty$ (cyan), and convex polyhedra with $N_c = 10$ (dark blue), $N_c = 100$ (green), and $N_c = 1,000$ (purple). Crosses denote the arithmetic mean over five geometric realizations (except for the cube) and the bars indicate the range between the minimum and the maximum value.

Gaussian random cubes behave entirely differently from the convex polyhedra considered in the previous section. While the optical properties of the polyhedra scatter about the reference values of cubes, the Gaussian random cubes introduce a bias in the linear depolarization ratio; they all increase $\delta_l$relative to the reference values for cubes. The small scale distortions ($\Gamma = 10°, 20°, 30°$) result in depolarization ratios, that deviate more strongly from the values obtained for cubes than the depolarization ratios stemming from the large scale distortion ($\Gamma = 90°$). The consequences of these results will be discussed in Section 5.

4.3. Superellipsoids

Figure 15 shows the (11) (top row), (22) (middle row), and (12) (bottom row) elements of the scattering matrix F for superellipsoids with different roundness parameter, as indicated by the colors. Shades of green indicate (rounded) cubes, while shades of purple indicate (rounded) octahedra. The (22) and (12) elements are normalized with respect to the (11) element. The columns indicate the different sizes, with the results for $r_{ve} = 0.25$ μm shown in the left column, for $r_{ve} = 0.5$ μm in the middle column, and for $r_{ve} = 1.0$ μm in the right column.

Scattering matrix elements for cubes with sharp edges do not strongly differ from those with rounded edges. Similarly, octahedra with sharp and with rounded edges display many similarities. The differences between cube-like and octahedra-like particles are generally larger than the corresponding differences among particles with different degrees of roundness in each of these two groups.

Analogous to Figure 10, Figure 16 shows the size-dependent backscattering cross section C_{bak} (top row), the size-dependent extinction-to-backscatter ratio S_p (middle row), and the linear backscattering depolarization ratio δ_l (bottom row). The different colors refer to the superellipsoids with different roundness parameters n with colors as in Figure 15. The values shown in Figure 16 are also tabulated in Table S3.

For $r_{ve} = 1.0$ μm (rounded) octahedra have a higher backscattering cross section than (rounded) cubes, which results in a lower extinction-to-backscatter ratio. Furthermore, the values of the linear depolarization ratio from (rounded) cubes ($\delta_l \approx 0.22$) and (rounded) octahedra ($\delta_l \sim 0.35$–0.4) for $r_{ve} = 1.0$ μm deviate more strongly from each other, than for the other two sizes. Increasing roundness, that is, values of the roundness parameter
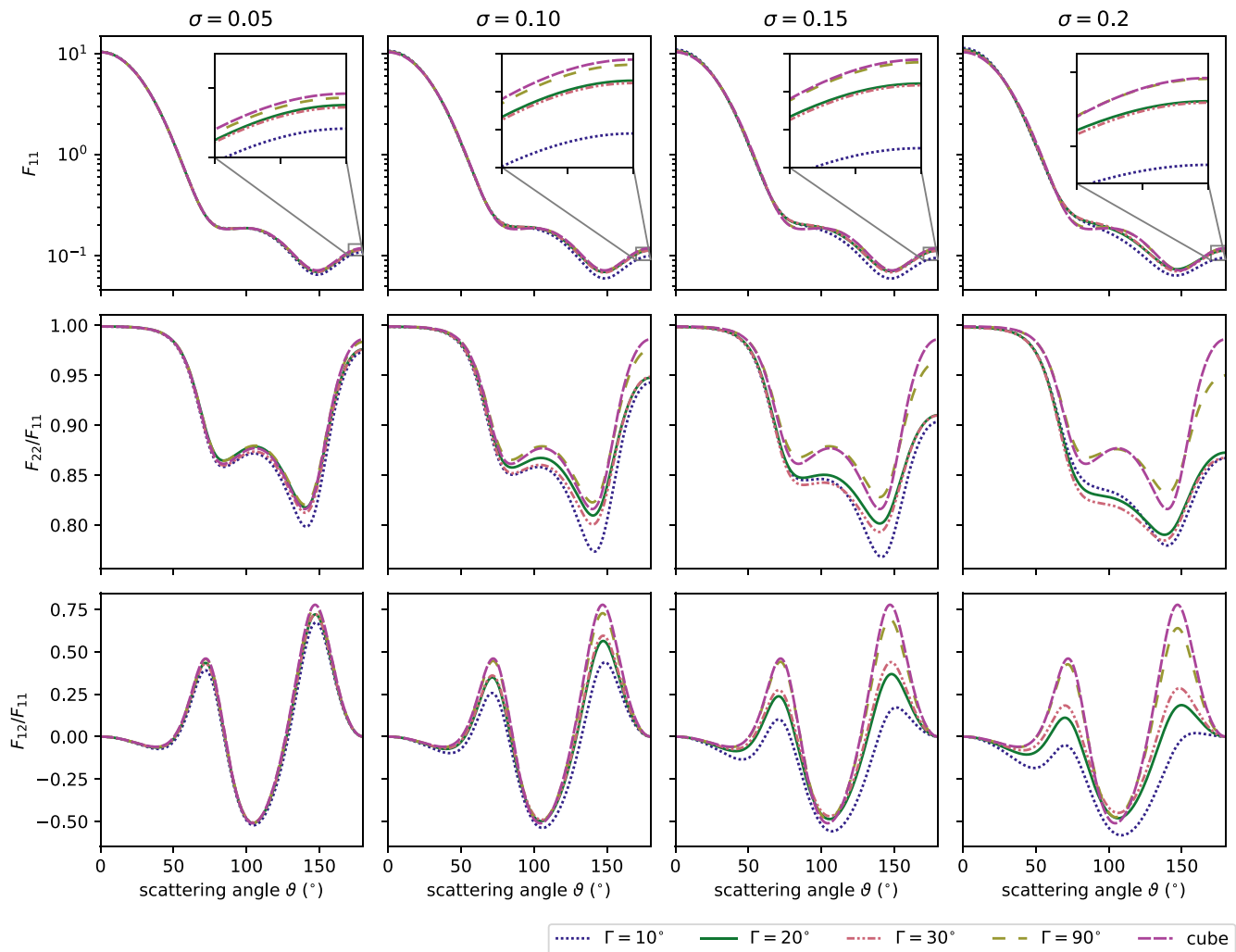
Figure 11. Ensemble-mean of F_{11} (top row), F_{22} (center row), and F_{12} (bottom row) scattering matrix elements for Gaussian random cubes with a volume equivalent radius of $r_{ve} = 0.25\ \mu m$ and different correlation angle Γ (indicated by the colors) and radial standard deviation σ_r (columns). In each plot the corresponding elements of a cube (purple line) were added for comparison. The left columns shows results for $\sigma_r = 0.05$, the center left for $\sigma_r = 0.1$, the center right for $\sigma_r = 0.15$, and the right column for $\sigma_r = 0.2$. A correlation angle of $\Gamma = 10°$ is indicated by the dark blue lines, $\Gamma = 20°$ by green, $\Gamma = 30°$ by light red, and $\Gamma = 90°$ by yellow.

closer to 1, generally decreases the linear depolarization ratio. With exception of the octahedron-like superellipsoids with $r_{ve} = 1.0\ \mu m$, for which the depolarization ratio was increased with increasing roundness.

The results, so far, provide us with valuable information on the importance of overall shape and roundness for modeling optical properties of marine aerosol. However, they are based on comparing model particles with a definite size. We now want to turn our attention to size-averaged optical properties of ensembles of randomly oriented cubes with varying degrees of roundness. We also consider three different refractive indices as explained in Sec. 3. These results have been computed with the T-matrix program Tsym.

Figure 17 shows the backscattering cross section (top), the lidar ratio (center), and the linear backscattering depolarization ratio (bottom) as a function of the effective radius. The lines represent different model particles as indicated in the legend and figure caption. Comparison of the left and right column shows that the results hardly depend on whether we assume a monomodal (left) or a bimodal (right) size distribution. (Note the different ranges on the x-axis in either column.)
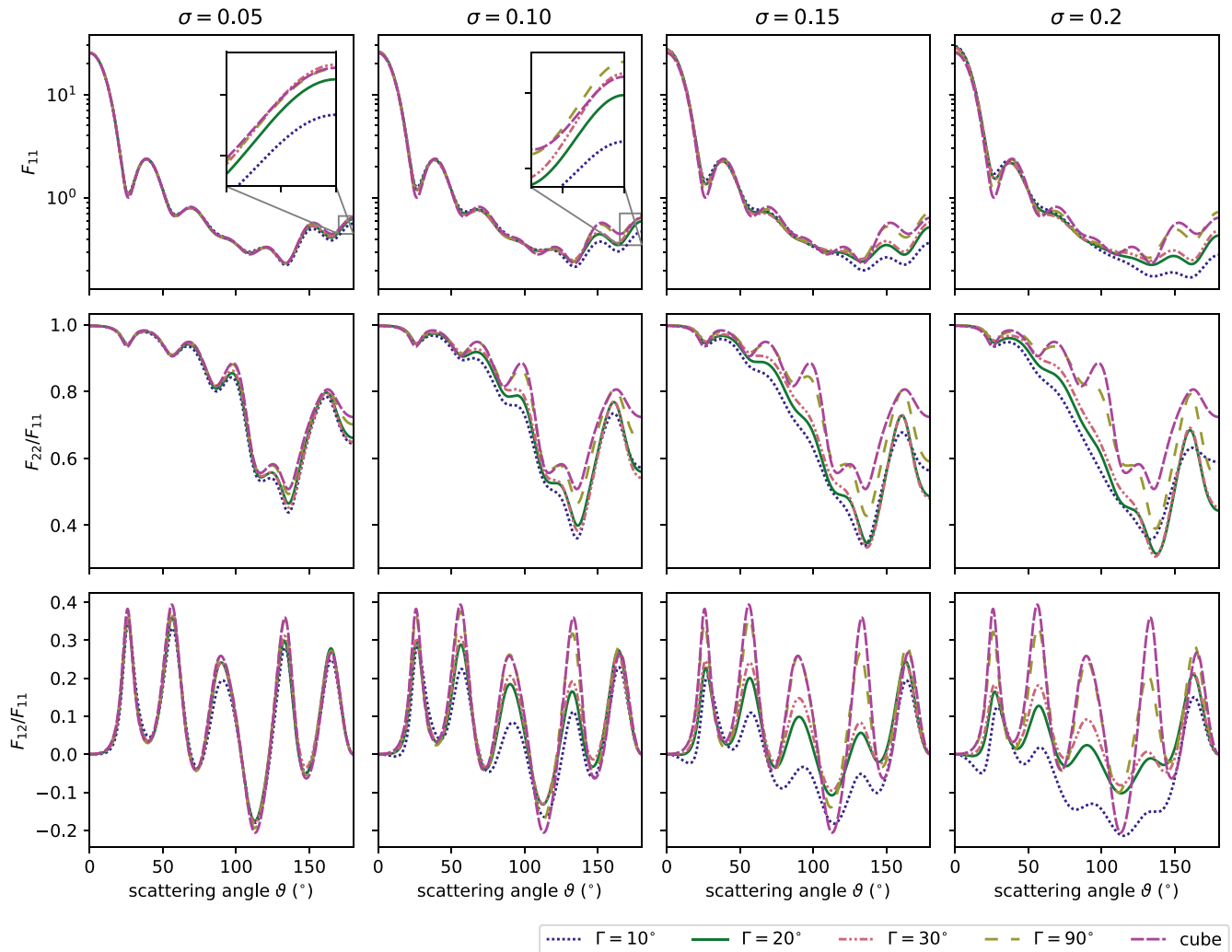
Figure 12. As Figure 11, but for a volume-equivalent radius of $r_{ve} = 0.5$ μm.

Most prominently, we see that the impact of roundness on C_{bak} and S_p is dwarfed by that of the imaginary part κ of the refractive index. Increasing κ from 0 to 0.06 results in a dramatic decrease in C_{bak}, which causes a strong increase in S_p. The strength of this effect grows with increasing r_{eff}. By contrast, the corresponding impacts on δ_l are considerably more complex. The impact of roundness is, generally, of comparable magnitude as that of absorption. While roundness generally lowers δ_l for $r_{eff} \leq 1.3$, μm relative to cubes with sharp edges, it can have a lowering effect for $r_{eff} > 1.3$, μm and $e = n = 0.1$, and an enhancing effect for $e = n = 0.2$. A change in the refractive index from 1.55 to 1.415 + 0.002i enhances depolarization over the entire size range (compare the green and the magenta curves). An increase of κ from 0 to 0.06 has little effect for $r_{eff} \leq$ 0.9, μm, after which δ_l strongly drops with growing r_{eff} (compare the green and red curves).

A possible explanation for the latter effect is this. Depolarization by nonspherical particles is strongly influenced by internal resonances induced inside the particle by the incident electromagnetic field. In absorbing particles, these resonances can become quenched. With growing size the absorption cross sections increases, which gradually diminishes the impact of the internal resonance modes. This mainly leaves induced surface currents on the particle surface to impact the depolarization properties of the particle. It is conceivable that the effect of these currents is weaker than that of the resonant modes inside the particle, which would explain the decrease in δ_l with growing particle size.
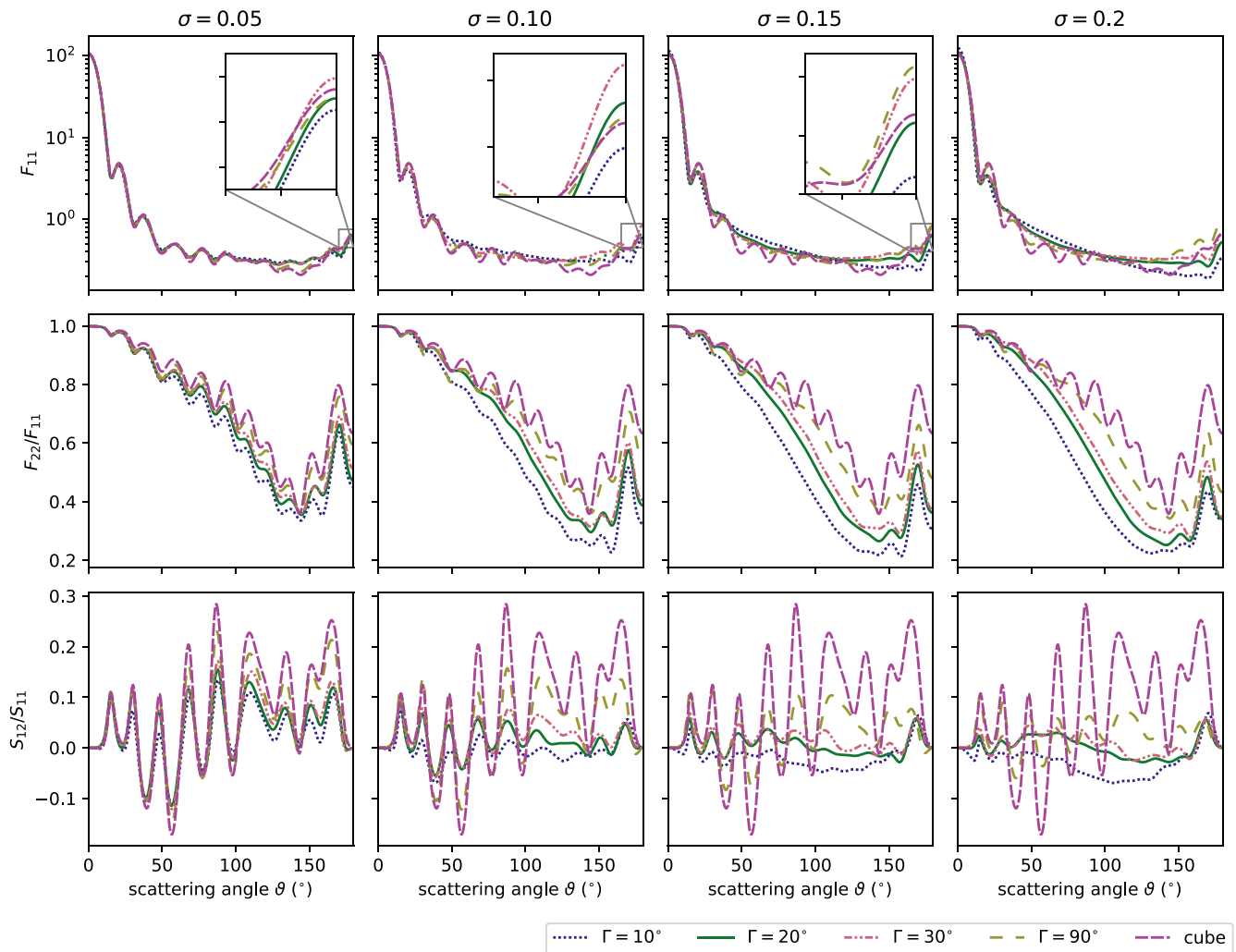
Figure 13. As Figure 11, but for a volume-equivalent radius of $r_{ve} = 1.0$ μm.

Figure 18 shows elements of the size-averaged Stokes scattering matrix as a function of scattering angle (x-axis) and effective radius (y-axis). A comparison with Figure 15 shows that size-averaging smooths out many of the resonance features encountered for monodisperse particles, especially for larger particles. Comparison of rows 1 and 2 reveals that the rounding of the edges has a rather small effect on both the (11) element (left) and the (12) element (right), and a somewhat more pronounced effect on the (22) element (center column), especially at scattering angles around 100°–150°. By contrast, comparison of rows 1, 3, and 4 shows that a change in the refractive index, especially an increase in its imaginary part (row 4) has a dramatic effect on the (22) and (12) elements. In the (22) element, the deep minimum at scattering angles between 100° and 150° becomes considerably more flat with increasing absorption. In the (12) element there is a fairly shallow minimum at scattering angles around 40° for non-absorbing, large particles (top right). As the particles become absorbing, this minimum deepens and shifts toward a scattering angle around 60° (bottom right).

5. Discussion and Conclusions

Here, we want to discuss our results with a tight focus on the three questions we initially posed in the introduction to this article. But before doing this, a few words on the rationale behind the use of superellipsoidal model particles are in order. As demonstrated by Bi, Lin, Liu, et al. (2018), this model covers a large range
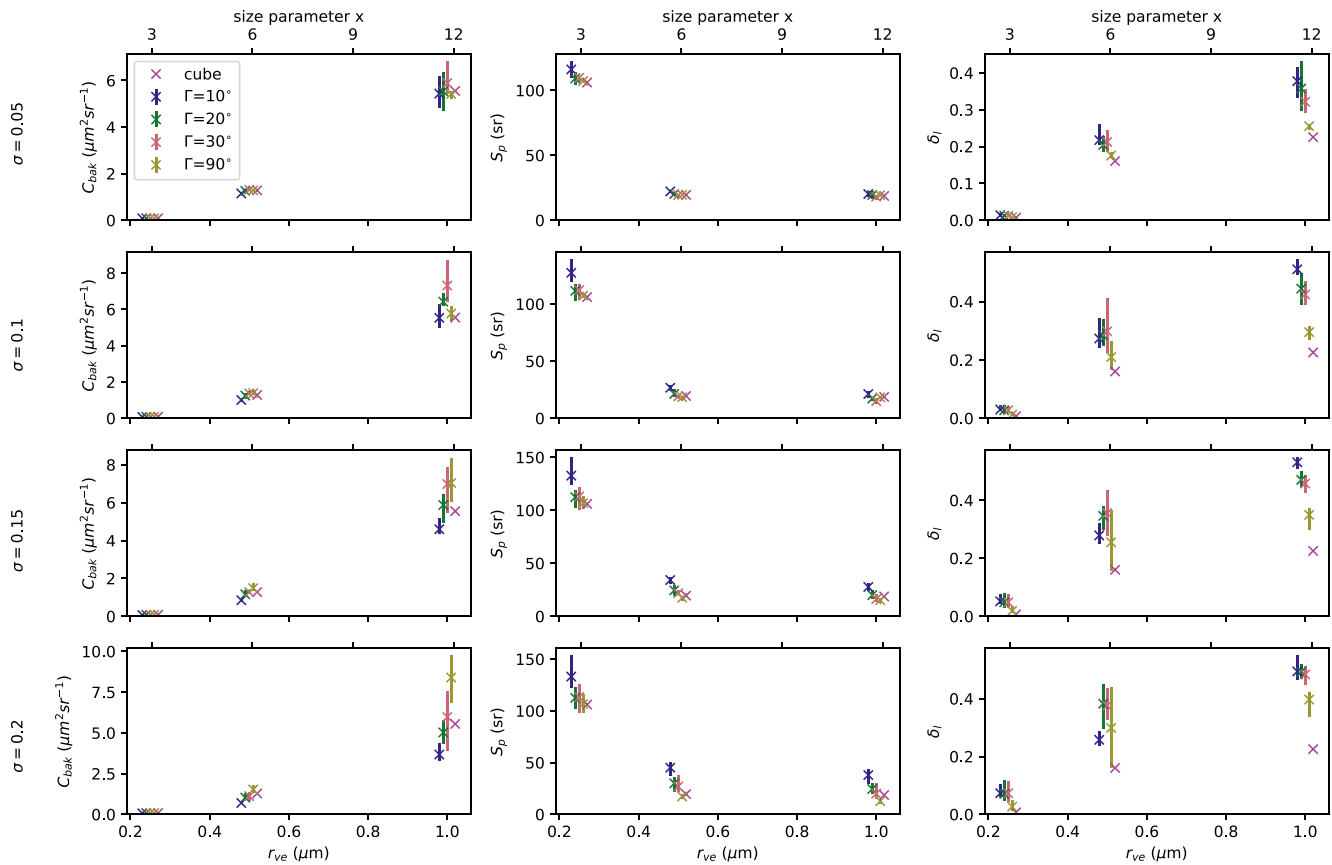
Figure 14. Size-dependent backscattering cross sections C_{bak} (left column), extinction-to-backscatter ratios S_p (middle column), and linear depolarization ratio δ_l (right column) of Gaussian random cubes with different correlation angle Γ and radial standard deviation σ_r. The different values of Γ are indicated by color (with colors as in Figure 11), and the different values of σ_r are presented in different rows (first row: $\sigma_r = 0.05$, second row: $\sigma_r = 0.1$, third row: $\sigma_r = 0.15$, and bottom row: $\sigma_r = 0.2$). For comparison, each panel shows the corresponding values of cubes in purple. Crosses denote the arithmetic mean over five geometric realizations (except for the cube) and the bars indicate the range between the minimum and the maximum value.

of depolarization ratios by varying the aspect ratio and the roundness parameters—see Figure 6b in their paper. Thus, it satisfies the third criterion of a versatile model particle as stated in the introduction. However, superellipsoids also introduce a large number of free parameters (two roundness and two aspect ratios). Thus, they seem to violate the second criterion. For this reason, we limit the number of free parameters by setting the two roundness parameters equal to each other, $n = e$, and by fixing the two aspect ratios, $a/b = a/c = 1$. This leaves us with a single free parameter, the roundness parameter n. This subset of superellipsoids comprises cubes and rounded cubes (as well as octahedra and rounded octahedra). Marine aerosols are dominated by sodium chloride, for which cubes are a canonical reference shape. Thus, model particles that bear a close resemblance to perfect cubes are an obvious choice in this case. We have, therefore, mainly considered superellipsoids that deviate only mildly from this reference geometry (with the exception of the octahedral particles).

Our first question is whether superellipsoids can be used to simultaneously simulate the depolarization ratio and the lidar ratio of marine aerosol. Our findings are best illustrated in the right column of Figure 17. The effective radii considered here (1.0–1.6 μm) cover a range typical for marine aerosol in the atmosphere at low to moderate wind speeds. (Note that the size distribution in (Bi, Lin, Liu, & Zhang, 2018) had a mean geometric radius of only 0.1 μm, which was selected in order to reproduce laboratory measurements by (Sakai et al., 2010)). In our simulations, the depolarization ratio of non-absorbing marine aerosols (black, blue, and green lines) varies with size and roundness parameter in the range $\delta_l = 0.14$–0.20, while the lidar ratio varies between $S_p = 12$–20 sr. This does lie within the range of reported field measurements listed in Table 1, which is an encouraging result. Optically softer, weakly absorbing aerosols (purple line) vary
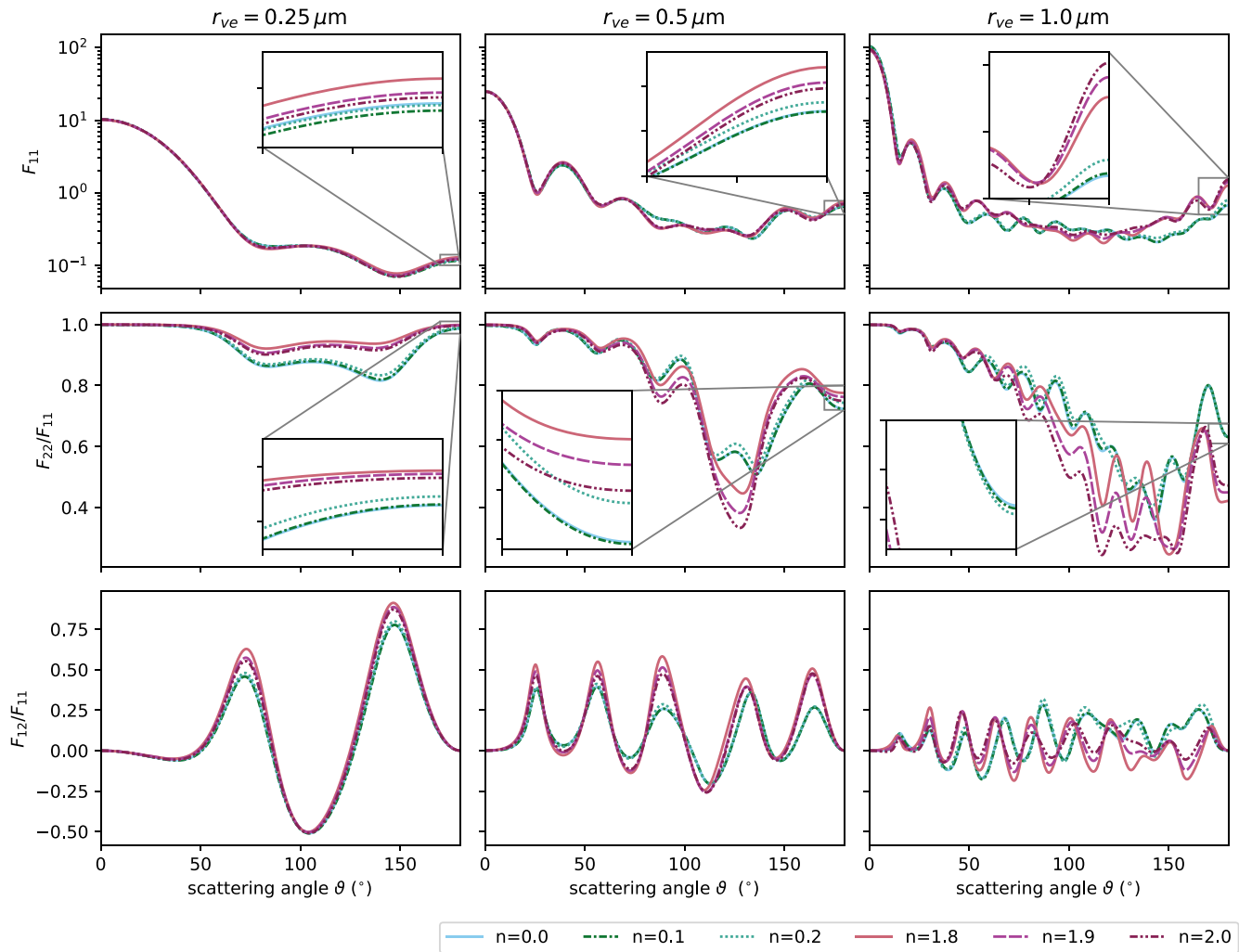
Figure 15. (11) (top row), (22) (center row), and (12) (bottom row) elements of the normalized scattering matrix F for different superellipsoids with $n = e = 0.0$, corresponding to a cube (cyan), $n = e = 0.1$ (dark green), $n = e = 0.2$ (light green), $n = e = 1.8$ (light red), $n = e = 1.9$ (purple), and $n = e = 2.0$, corresponding to a octahedron (wine). The (22) and (12) elements are normalized with respect to the (11) element. The columns represent the three different volume-equivalent radii $r_{ve} = 0.25\,\mu m$ (left column), $r_{ve} = 0.5\,\mu m$ (center column), and $r_{ve} = 1.0\,\mu m$ (right column).

between $\delta_l = 0.17$–0.22 and $S_p = 25$–33 sr. The depolarization ratios are still in the range of reported field values, while the lidar ratios are at and above the high end. It is possible that a real part of the refractive index of 1.415, which is even lower than that of pure DMS, is untypically low for marine aerosol. Clearly, for gaining more confidence in the superellipsoid model it will be highly desirable to obtain more simultaneous field measurements of δ_l and S_p, as well as a more clearly defined range of typical values of the refractive index.

A geometrically idealized model, such as superellipsoids, is not expected to accurately reproduce each and every observation under atmospheric conditions. Rather, one aims at developing a model that will work on average. By this we mean that observations will scatter about the model predictions with a certain variance and, hopefully, with minimum bias. To employ such an optics model in inverse methods it is crucial to carefully quantify the model's error variance. Randomized geometries are the most promising candidates for obtaining realistic estimates of the error variance, as we know from detailed studies on mineral dust aerosols (Kahnert et al., 2020). Thus, our second question is which randomization model would be a good candidate for quantifying model errors. To address this question, we compare Figures 10 and 14.
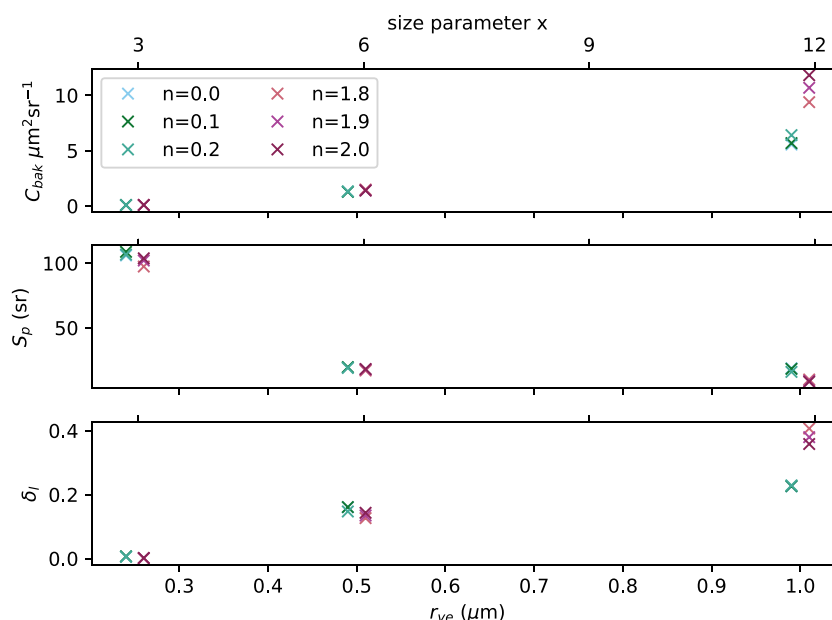
Figure 16. Size-dependent backscattering cross section C_{bak} (top row), extinction-to-backscatter ratio S_p (middle row), linear backscattering depolarization ratio δ_l (bottom row) for superellipsoids with different roundness parameters n. The colors are as in Figure 15. In order to distinguish the values more easily, the radius values were slightly shifted with respect to the x-axis.

The results obtained for convex polyhedra and for Gaussian random cubes could not have been more different. The ones for convex polyhedra in Figure 10 scatter about the reference results for cubes. There are deviations both among different stochastic realizations for fixed N_c as well as among different values of N_c. We note that polyhedra with $N_c = 10$ may be a bit of an extreme case that deviate substantially from cubes, while results obtained for $N_c = 1,000$ are very similar to cubes, and there is hardly any stochastic variation in the optical properties among different realizations of the geometry. By contrast, prisms with $N_c = 100$ seem to provide a good model for simulating random errors related to the geometric variability of marine aerosol. A promising approach may be to combine prisms generated for different values of N_c in the vicinity of 100 with different stochastic realizations of the geometry.

By contrast, Gaussian random surface perturbation (Figure 14) significantly increase δ_l relative to the cubical reference particles. The larger the radial standard deviation σ_r and the smaller the correlation angle Γ, the more the depolarization ratio is enhanced. Thus, this randomization model appears to be unsuitable for modeling random errors. This a remarkable and entirely unexpected result. It was earlier found that Gaussian random perturbations of spheroids are an excellent approach to model the error variance of the spheroid model for mineral dust (Kahnert et al., 2020).

Our third question is how the sensitivity of the optical properties due to variations in geometry and due to variations in the dielectric properties compare to each other. Returning to Figure 17, we see that both δ_l and S_p vary significantly with refractive index. A reduction of the real part from 1.55 to 1.415 can significantly enhance both δ_l and S_p. An increase in the imaginary part can strongly reduce δ_l while enhancing S_p. We learn from this that the refractive index is both an important tuning parameter of the model, and an essential source of uncertainty that needs to be accounted for in the error estimates. However, more reliable information from observations would be needed to narrow down the range of real and imaginary parts of the refractive index that can be considered representative for marine aerosol.

In conclusion, we find that superellipsoids that resemble cubes with rounded edges are a promising candidate for simultaneously modeling the backscattering coefficient and the lidar ratio of dry ma-
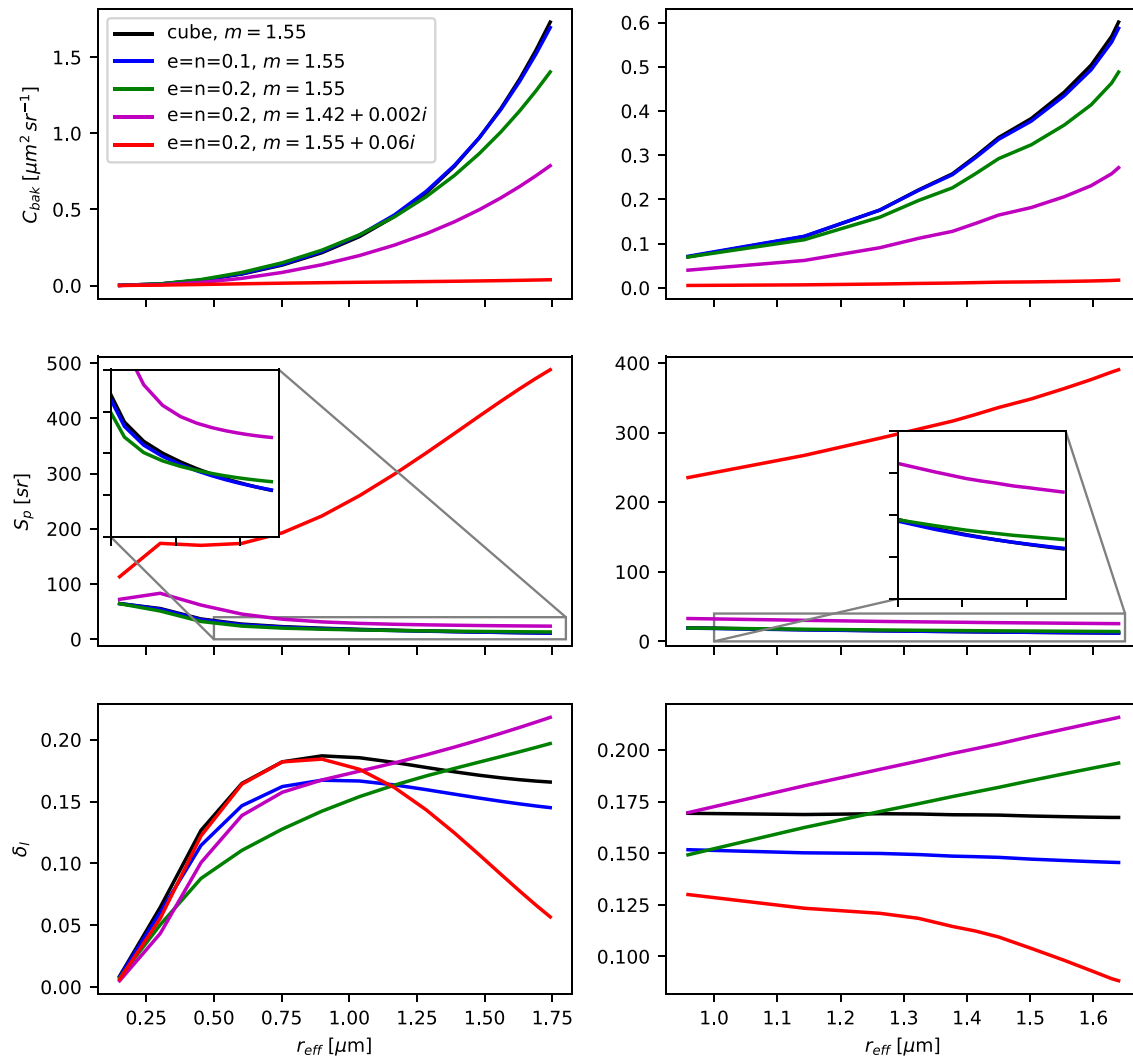
Figure 17. Size-averaged results for C_{bak} (top), S_p (center), and δ_l (bottom) as a function of the effective radius r_{eff}. The lines show non-absorbing cubes with sharp edges (black), non-absorbing cubic superellipsoids with $e = n = 0.1$ (blue) and $n = e = 0.2$ (green), as well as superellipsoids ($e = n = 0.2$) with refractive indices $m = 1.415 + 0.002i$ (magenta) and $m = 1.55 + 0.06i$ (red). The left row shows results averaged over log-normal monomodal size distributions, the right one over bimodal log-normal size distributions as explained in the text.

rine aerosol. Our results support this conclusion for effective radii that are representative for marine aerosol generated at low to moderate wind speed. Further studies will need to rely on more extensive data from measurements for comparison. Randomized cuboidal polyhedra can be a useful model for simulating model uncertainties. Gaussian random perturbations of a cube result in an enhancement of the depolarization ratio rather than in random variations. Therefore, this model does not seem to be suitable for simulating random errors. The uncertainty in the refractive index strongly impacts the optical properties and needs to be accounted for in the error estimates. It is highly desirable to obtain more observation-based information to constrain the range of realistic values of the refractive index of marine aerosol.

Here, only crystalline sea-salt aerosol without any water coating was investigated. Adding a liquid water coating would extend the applicability of the irregular model particles in the ADDA computations discussed here towards higher values of relative humidity. Further laboratory studies combining measurements of the optical and the microphysical properties of dried sea-salt aerosol particles can provide additional guidance regarding the choice and/or refinement of particle models.
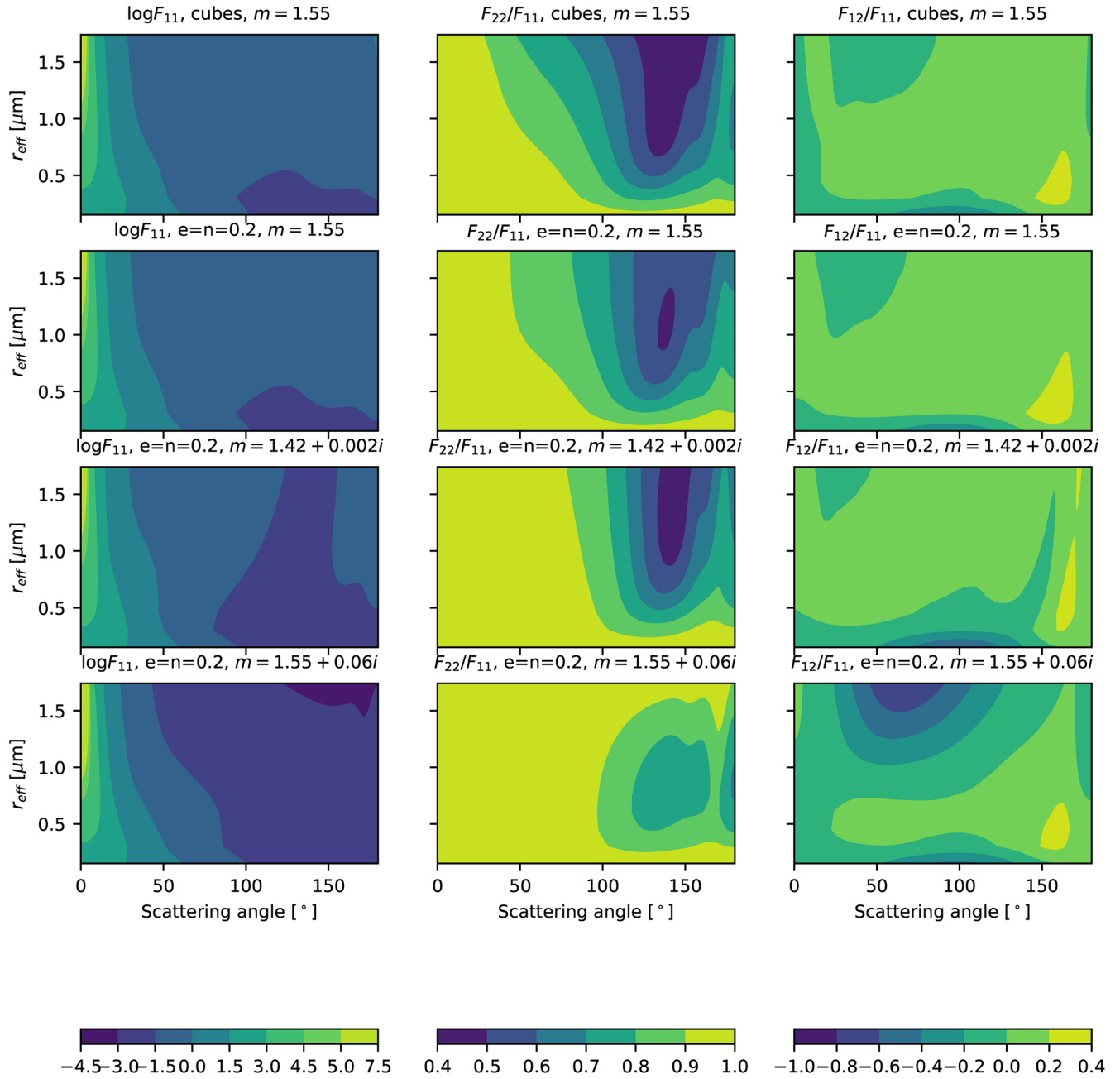
Figure 18. Elements of the Stokes scattering matrix as a function of scattering angle and effective radius r_{eff}. The three columns show the elements $\log F_{11}$ (left), F_{22}/F_{11} (center), and F_{12}/F_{11} (right). The rows show results for refractive indices $m = 1.55$ (rows 1 and 2), $1.415 + 0.002i$ (row 3), and $1.55 + 0.06i$ (row 4), as well as for roundness parameters $e = n = 0$ (rows 1) and $e = n = 0.2$ (row 2–4).

Appendix A: Parameterization of Superellipsoids in Spherical Coordinates

In Waterman's T-matrix method, we need to evaluate vector products of vector spherical wavefunctions $\psi_{l,m,q}^{(j)}\left(r(\theta,\phi),\theta,\phi\right)$, where l, m, q are the degree, order, and mode, and where j denotes the kind of the vector wavefunctions. The surface integrals are evaluated at the surface $r(\theta, \phi)$ of the particle. Thus, to use Waterman's method we need to have a parameterization of the particle surface in spherical coordinates, as well as the parameterization's partial derivatives. We are not aware of any publications that present such a

parameterization, certainly not in the light-scattering literature. Thus, we derive this parameterization here in the appendix.

We start from the implicit Equation 2 for the surface of a superellipsoid given in Cartesian coordinates by

$$\left(\left| \frac{x}{a} \right|^{2/e} + \left| \frac{y}{b} \right|^{2/e} \right)^{e/n} + \left| \frac{z}{c} \right|^{2/n} = 1. \tag{A1}$$

The parameters a, b, c, n, and e are positive real numbers. a, b, and c characterize the extent of the particle along the three Cartesian axes, n is a roundness parameter in the polar (north-south) direction, and e is a roundness parameter in the azimuthal (east-west) direction. The superellipsoids are convex for n, $e \in (0, 2)$.

An explicit surface parameterization of superellipsoids can be found in, for example, Wriedt (2002). That parameterization can be stated somewhat more rigorously by introducing the following bracket notation:

$$[\xi]^{\alpha} = \text{sgn}(\xi) \mid \xi \mid^{\alpha} . \tag{A2}$$

Then an explicit parameterization is given by

$$x = a[\cos u]^{n}[\cos v]^{e} \tag{A3}$$

$$y = b[\cos u]^{n}[\sin v]^{e} \tag{A4}$$

$$z = c[\sin u]^{n} \tag{A5}$$

$$u \in [-\pi / 2, \pi / 2], \ v \in [-\pi, \pi]. \tag{A6}$$

It is elementary to verify by direct substitution into Equation (A1) that this parameterization, indeed, describes the surface of a superellipsoid. However, (u, v) are not spherical coordinates, as required by Waterman's T-matrix method.

To derive a parameterization in spherical coordinates (θ, ϕ), we need a parameter transformation $(u, v) \mapsto (\theta, \phi)$. To this end, we compute

$$\frac{y}{x} = \tan \phi = \frac{b}{a}[\tan(v - k\pi)]^{e}, \quad k \in \mathbb{Z}, \tag{A7}$$

or

$$\tan(v - k\pi) = \left[\frac{a}{b} \tan \phi \right]^{1/e}, \tag{A8}$$

where we explicitly indicated the periodicity of the tangent. The choice of k becomes important when computing $\phi = \arctan(y/x)$. Making appropriate case distinctions for the four quadrants, we find that $k = 0$ for $\phi \in [0, \pi/2)$, $k = 1$ for $\phi \in [\pi/2, \pi)$, $k = -1$ for $\phi \in [\pi, 3\pi/2)$, and $k = -2$ for $\phi \in [3\pi/2, 2\pi)$. Thus we obtain the following parameter transformation

$$v(\phi) = \arctan\left(\left[\frac{a}{b} \tan \phi \right]^{1/e} \right) + k\pi \tag{A9}$$

$$
k \;=\; \begin{cases} 0 &:\quad \phi \in [0,\pi/2) \\ 1 &:\quad \phi \in [\pi/2,\pi) \\ -1 &:\quad \phi \in [\pi,3\pi/2) \\ -2 &:\quad \phi \in [3\pi/2,2\pi) \end{cases} \tag{A10}
$$

To obtain an analogous parameter transformation for u, we consider

$$
\frac{\sqrt{x^2+y^2}}{z} = \tan\theta = \frac{1}{c}\frac{[\cos u]^n}{[\sin u]^n}\left\{ a^2 \mid\cos v\mid^{2e} + b^2\mid\sin v\mid^{2e}\right\}^{1/2}, \tag{A11}
$$

or

$$
[\tan u]^n = \frac{1}{c}\cot\theta\sqrt{w}, \tag{A12}
$$

where

$$
w(v(\phi)) = a^2 \mid\cos v\mid^{2e} + b^2\mid\sin v\mid^{2e} \tag{A13}
$$

To solve for u, we make a case distinction. For $\theta \in [0,\pi/2)$, $\cot\theta > 0$. Then we must have $\tan u > 0$, which implies $u \in [0,\pi/2)$. Then $u = \arctan\{(1/c)\cot\theta\sqrt{w}\}^{1/n}$. Similarly, for $\theta \in [\pi/2,\pi)$ we find $u = -\arctan\{-(1/c)\cot\theta\sqrt{w}\}^{1/n}$. This can be summarized as follows

$$
u(\theta,\phi) \;=\; S\arctan\left\{ \frac{S}{c}\cot\theta\sqrt{w(v(\phi))}\right\}^{1/n} \tag{A14}
$$

$$
S \;=\; \begin{cases} 1 &:\quad \theta \in [0,\pi/2) \\ -1 &:\quad \theta \in [\pi/2,\pi) \end{cases} \tag{A15}
$$

Equations A9 and A14 in conjunction with Equations A10, A13, and A15 provide us with the desired parameter transformation $(u,v)\mapsto(\theta,\phi)$. Substitution into Equations A3–A5 in conjunction with $r=\sqrt{x^2+y^z+z^2}$ gives us the required parameterization $r(\theta,\phi)$ of the superellipsoid surface in spherical coordinates.

To evaluate the surface integrals in Waterman's method, we also need to express the surface element $d\sigma$ on the surface of the particle in spherical coordinates, that is, we need to obtain $d\sigma = |\partial\mathbf{r}/\partial\theta \times \partial\mathbf{r}/\partial\phi|\,d\theta\,d\phi$. In principle, we could now proceed and compute expressions such as $\partial r/\partial\theta = (\partial r/\partial u)\,(\partial u/\partial\theta)$. It turns out that we encounter singularities in terms such as $\partial u/\partial\theta$. Therefore, we do well to first bring the parameter transformations into a more tractable form.

Inspection of Equations A3–A5 shows that we never need the parameters u and v directly, but only $\cos u$, $\sin u$, $\cos v$ and $\sin v$. We can make use of the identities

$$
\sin(\arctan x) \;=\; \frac{x}{\sqrt{1+x^2}} \tag{A16}
$$

$$
\cos(\arctan x) \;=\; \frac{1}{\sqrt{1+x^2}}, \tag{A17}
$$

and we abbreviate

$$
p \;=\; \left\{ S\frac{\sqrt{w}}{c}\cot\theta\right\}^{1/n} = \left[\frac{\sqrt{w}}{c}\cot\theta\right]^{1/n} \tag{A18}
$$

$$q = \left[\frac{a}{b}\tan\phi\right]^{1/e}.$$
(A19)

This yields

$$\sin u = S\frac{p}{\sqrt{1+p^2}}$$
(A20)

$$\cos u = \frac{1}{\sqrt{1+p^2}}$$
(A21)

$$\sin v = (-1)^m\frac{q}{\sqrt{1+q^2}}$$
(A22)

$$\cos v = (-1)^m\frac{1}{\sqrt{1+q^2}},$$
(A23)

whence

$$w = \frac{a^2 + b^2(q^2)^e}{(1+q^2)^e}.$$
(A24)

and

$$
\begin{aligned}
r^2 &= x^2 + y^2 + z^2 \\
&= |\cos u|^{2n}(a^2|\cos v|^{2e} + b^2|\sin v|^{2e}) + c^2|\sin u|^{2n} \\
&= \frac{w + c^2(p^2)^n}{(1+p^2)^n},
\end{aligned}
$$
(A25)

where we have used the definition of w in Equation A13 as well as Equations A20 and A21. Backsubstitution of the definitions of p and q, Equations A18 and A19, into these expressions yields

$$r(\theta,\phi) = \left\{\frac{w}{\left\{(\sin^2\theta)^{1/n} + \left(\frac{w}{c^2}\cos^2\theta\right)^{1/n}\right\}^n}\right\}^{1/2}$$
(A26)

$$w(\phi) = \frac{a^2(1 + \tan^2\phi)}{\left\{1 + \left(\frac{a^2}{b^2}\tan^2\phi\right)^{1/e}\right\}^e}.$$
(A27)

The expression for r is manifestly regular for all θ. (Recall that $n > 0$.) Also, as we approach a singularity of $\tan\phi$, w approaches b^2. Thus, w and r are regular for all values of ϕ.

It is now straightforward, although a bit lengthy, to compute $\partial r/\partial\theta$ and $\partial r/\partial\phi = (\partial r/\partial w)\,(\partial w/\partial\phi)$. With the abbreviation

$$t = \tan^2\phi, \tag{A28}$$

The final result is

$$\frac{\partial r}{\partial\theta} = -\frac{w}{r}\frac{\cos\theta[\sin\theta]^{\frac{2}{n}-1} - \left(\frac{w}{c^2}\right)^{1/n}\sin\theta[\cos\theta]^{\frac{2}{n}-1}}{\left\{(\sin^2\theta)^{1/n} + \left(\frac{w}{c^2}\cos^2\theta\right)^{1/n}\right\}^{n+1}} \tag{A29}$$

$$\frac{\partial r}{\partial\phi} = \frac{a^2}{r}\frac{(\sin^2\theta)^{1/n}}{\left\{(\sin^2\theta)^{1/n} + \left(\frac{w}{c^2}\cos^2\theta\right)^{1/n}\right\}^{n+1}}\sqrt{t}\,(1+t)\frac{1 - \left(\frac{a^2}{b^2}\right)^{1/e}t^{\frac{1}{e}-1}}{\left\{1 + \left(\frac{a^2}{b^2}t\right)^{1/e}\right\}^{e+1}} \tag{A30}$$

$\partial r/\partial\phi$ is regular for all values of θ. $\partial r/\partial\theta$ is also regular for all θ, provided that $n < 2$. Further, it is straightforward to show that the term dependent on $t = \tan^2\phi$ approaches 0 as $t \to \infty$ provided that $e < 2$. Thus, for convex particles ($0 < n, e < 2$) the partial derivatives of r are regular for all values of θ and ϕ.

The surface parameterizations derived here, as well as their partial derivatives, have been implemented into the most recent version of the Tsym program. In order to compute the volume-equivalent radius of the particles, one needs the volume of the superellipsoids, which is given by Wriedt ([2002](#))

$$V = abcne B\left(\frac{n}{2}+1,n\right)B\left(\frac{e}{2},\frac{e}{2}\right), \tag{A31}$$

where the beta function B is defined in terms of the gamma function Γ according to

$$B(x,y) = \frac{\Gamma(x)\Gamma(y)}{\Gamma(x+y)}. \tag{A32}$$

Data Availability Statement

The data shown in the figures are available under: http://doi.org/10.5281/zenodo.3977897. The release version of the Tsym code is publicly available under http://doi.org/10.5281/zenodo.4304389. Access to the most recent version Tsym 6.6α that contains the superellipsoids can be obtained by contacting the authors.

References

Adachi, K., & Buseck, P. R. (2015). Changes in shape and composition of sea-salt particles upon aging in an urban atmosphere. *Atmospheric Environment*, *100*, 1–9. https://doi.org/10.1016/j.atmosenv.2014.10.036

Barber, C. B., Dobkin, D. P., & Huhdanpaa, H. (1996). The quickhull algorithm for convex hulls. *ACM Transactions on Mathematical Software*, *22*(4), 469–483. https://doi.org/10.1145/235815.235821

Barr, A. H. (1981). Superquadrics and angle-preserving transformations. *IEEE Computer Graphics and Applications*, *1*(1), 11–23. https://doi.org/10.1109/MCG.1981.1673799

Bi, L., Lin, W., Liu, D., & Zhang, K. (2018). Assessing the depolarization capabilities of nonspherical particles in a super-ellipsoidal shape space. *Optics Express*, *26*(2), 1726–1742. https://doi.org/10.1364/OE.26.001726

Bi, L., Lin, W., Wang, Z., Tang, X., Zhang, X., & Yi, B. (2018). Optical modeling of sea salt aerosols: The effects of nonsphericity and inhomogeneity. *Journal of Geophysical Research*, *123*(1), 543–558. https://doi.org/10.1002/2017JD027869

Bi, L., Yang, P., Kattawar, G., & Mishchenko, M. I. (2013). Efficient implementation of the invariant imbedding t-matrix method and the separation of variables method applied to large nonspherical inhomogeneous particles. *Journal of Quantitative Spectroscopy & Radiative Transfer*, *116*, 169–183.

Bohlmann, S., Baars, H., Radenz, M., Engelmann, R., & Macke, A. (2018). Ship-borne aerosol profiling with lidar over the atlantic ocean: From pure marine conditions to complex dust–smoke mixtures. *Atmospheric Chemistry and Physics*, *18*(13), 9661–9679. https://doi.org/10.5194/acp-18-9661-2018

Boucher, O. (2015). *Atmospheric aerosols - properties and climate impacts*. Dordrecht: Springer. https://doi.org/10.1007/978-94-017-9649-1

Buseck, P. R., & Pósfai, M. (1999). Airborne minerals and related aerosol particles: Effects on climate and the environment. *Proceedings of the National Academy of Sciences of the United States of America*, *96*(7), 3372–3379.

Carrillo, J., Guerra, J. C., Cuevas, E., & Barrancos, J. (2016). Characterization of the marine boundary layer and the trade-wind inversion over the sub-tropical north atlantic. *Boundary-Layer Meteorology*, *158*(2), 311–330. https://doi.org/10.1007/s10546-015-0081-1

Chamaillard, K., Kleefeld, C., Jennings, S., Ceburnis, D., & O'Dowd, C. (2006). Light scattering properties of sea-salt aerosol particles inferred from modeling studies and ground-based measurements. *Journal of Quantitative Spectroscopy & Radiative Transfer*, *101*(3), 498–511.(Light in Planetary Atmospheres and Other Particulate Media). https://doi.org/10.1016/j.jqsrt.2006.02.062

Chi, J. W., Li, W. J., Zhang, D. Z., Zhang, J. C., Lin, Y. T., Shen, X. J., et al. (2015). Sea salt aerosols as a reactive surface for inorganic and organic acidic gases in the arctic troposphere. *Atmospheric Chemistry and Physics*, *15*(19), 11341–11353. https://doi.org/10.5194/acp-15-11341-2015

Cooper, D., Davis, J., & Byers, R. (1974). Measurements of depolarization by dry and humidified salt aerosols using a lidar analogue. *Journal of Aerosol Science*, *5*(2), 117–123. https://doi.org/10.1016/0021-8502(74)90043-3

Cotterell, M. I., Willoughby, R. E., Bzdek, B. R., Orr-Ewing, A. J., & Reid, J. P. (2017). A complete parameterisation of the relative humidity and wavelength dependence of the refractive index of hygroscopic inorganic aerosol particles. *Atmospheric Chemistry and Physics*, *17*(16), 9837–9851. https://doi.org/10.5194/acp-17-9837-2017

David, G., Thomas, B., Nousiainen, T., Miffre, A., & Rairoux, P. (2013). Retrieving simulated volcanic, desert dust and sea-salt particle properties from two/three-component particle mixtures using uv-vis polarization lidar and t matrix. *Atmospheric Chemistry and Physics*, *13*, 6757–6776. https://doi.org/10.5194/acp-13-6757-2013

Draine, B. T., & Flatau, P. J. (1994). Discrete-dipole approximation for scattering calculations. *Journal of the Optical Society of America. A*, *11*(4), 1491–1499. https://doi.org/10.1364/JOSAA.11.001491

Eldridge, J., & Palik, E. D. (1997). Sodium chloride (nacl). In E. D. Palik (Ed.), *Handbook of optical constants of solids* (pp. 775–793). Burlington: Academic Press. https://doi.org/10.1016/B978-012544415-6.50041-8

Eloranta, E. E. (2005). High spectral resolution lidar. In C. Weitkamp (Ed.), *Lidar: Range-resolved optical remote sensing of the atmosphere* (pp. 143–163). New York, NY: Springer. https://doi.org/10.1007/0-387-25101-4_5

Foltescu, V., Pryor, S. C., & Bennet, C. (2005). Sea salt generation, dispersion and removal on the regional scale. *Atmospheric Environment*, *39*, 2123–2133.

Gasteiger, J., & Wiegner, M. (2018). Mopsmap v1.0: A versatile tool for the modeling of aerosol optical properties. *Geoscientific Model Development*, *11*(7), 2739–2762. https://doi.org/10.5194/gmd-11-2739-2018

Gasteiger, J., Wiegner, M., GroSS, S., Freudenthaler, V., Toledano, C., Tesche, M., & Kandler, K. (2011). Modelling lidar-relevant optical properties of complex mineral dust aerosols. *Tellus B*, *63*(4), 725–741. https://doi.org/10.1111/j.1600-0889.2011.00559.x

Groß, S., Esselborn, M., Weinzierl, B., Wirth, M., Fix, A., & Petzold, A. (2013). Aerosol classification by airborne high spectral resolution lidar observations. *Atmospheric Chemistry and Physics*, *13*(5), 2487–2505. https://doi.org/10.5194/acp-13-2487-2013

Gwaze, P., Helas, G. A., Annegarn, H. J., Huth, J., & Piketh, S. J. (2007). Physical, chemical and optical properties of aerosol particles collected over Cape Town during winter haze episodes. *South African Journal of Science*, *103*, 35–43.

Haarig, M., Ansmann, A., Gasteiger, J., Kandler, K., Althausen, D., Baars, H., et al. (2017). Dry versus wet marine particle optical properties: Rh dependence of depolarization ratio, backscatter, and extinction from multiwavelength lidar measurements during saltrace. *Atmospheric Chemistry and Physics*, *17*(23), 14199–14217. https://doi.org/10.5194/acp-17-14199-2017

Hänel, G. (1976). The properties of atmospheric aerosol particles as functions of the relative humidity at thermodynamic equilibrium with the surrounding moist air. In H. Landsberg, & J. V. Mieghem (Eds.), *Advances in Geophysics* (Vol. 19, pp. 73–188) Elsevier. https://doi.org/10.1016/S0065-2687(08)60142-9

Hess, M., Koepke, P., & Schult, I. (1998). Optical properties of aerosols and clouds: The software package opac. *Bulletin of the American Meteorological Society*, *79*(5), 831–844. https://doi.org/10.1175/1520-0477(1998)079⟨0831:OPOAAC⟩2.0.CO;2

Irshad, R., Grainger, R. G., Peters, D. M., McPheat, R. A., Smith, K. M., & Thomas, G. (2009). Laboratory measurements of the optical properties of sea salt aerosol. *Atmospheric Chemistry and Physics*, *9*(1), 221–230. https://doi.org/10.5194/acp-9-221-2009

Järvinen, E., Kemppinen, O., Nousiainen, T., Kociok, T., Möhler, O., Leisner, T., & Schnaiter, M. (2016). Laboratory investigations of mineral dust near-backscattering depolarization ratios. *Journal of Quantitative Spectroscopy & Radiative Transfer*, *178*, 192–208.(Electromagnetic and light scattering by nonspherical particles XV: Celebrating 150 years of Maxwell's electromagnetics). https://doi.org/10.1016/j.jqsrt.2016.02.003

Johnson, B. R. (1988). Invariant imbedding t matrix approach to electromagnetic scattering. *Applied Optics*, *27*(23), 4861–4873. https://doi.org/10.1364/AO.27.004861

Kahnert, M. (2005). Irreducible representations of finite groups in the T matrix formulation of the electromagnetic scattering problem. *Journal of the Optical Society of America. A*, *22*, 1187–1199.

Kahnert, M. (2013a). The T-matrix code Tsym for homogeneous dielectric particles with finite symmetries. *Journal of Quantitative Spectroscopy & Radiative Transfer*, *123*, 62–78.

Kahnert, M. (2013b). T-matrix computations for particles with high-order finite symmetries. *Journal of Quantitative Spectroscopy & Radiative Transfer*, *123*, 79–91.

Kahnert, M., & KanngieSSer, F. (2020). Modelling optical properties of atmospheric black carbon aerosols. *Journal of Quantitative Spectroscopy & Radiative Transfer*, *244*, 106849. https://doi.org/10.1016/j.jqsrt.2020.106849

Kahnert, M., Kanngießer, F., Järvinen, E., & Schnaiter, M. (2020). Aerosol-optics model for the backscatter depolarisation ratio of mineral dust particles. *Journal of Quantitative Spectroscopy & Radiative Transfer*, *254*, 107177. https://doi.org/10.1016/j.jqsrt.2020.107177

King, S. M., Butcher, A. C., Rosenoern, T., Coz, E., Lieke, K. I., de Leeuw, G., et al. (2012). Investigating primary marine aerosol properties: Ccn activity of sea salt and mixed inorganic-organic particles. *Environmental Science and Technology*, *46*(19), 10405–10412. https://doi.org/10.1021/es300574u

Krishnamurti, T. N., Stefanova, L., & Misra, V. (2013). *Tropical meteorology: An introduction*. New York, NY: Springer. https://doi.org/10.1007/978-1-4614-7409-8

McInnes, L. M., Covert, D. S., Quinn, P. K., & Germani, M. S. (1994). Measurements of chloride depletion and sulfur enrichment in individual sea-salt particles collected from the remote marine boundary layer. *Journal of Geophysical Research: Atmosphere*, *99*(D4), 8257–8268. https://doi.org/10.1029/93JD03453

Meira, G., Andrade, C., Alonso, C., Padaratz, I., & Borba, J. (2008). Modelling sea-salt transport and deposition in marine atmosphere zone – a tool for corrosion studies. *Corrosion Science*, *50*(9), 2724–2731. https://doi.org/10.1016/j.corsci.2008.06.028

Mishchenko, M. I., & Hovenier, J. W. (1995). Depolarization of light backscattered by randomly oriented nonspherical particles. *Optics Letters*, *20*(12), 1356–1358. https://doi.org/10.1364/OL.20.001356

Mishchenko, M. I., Travis, L. D., & Lacis, A. A. (2002). *Scattering, absorption, and emission of light by small particles*. Cambridge University Press.

Muinonen, K., Nousiainen, T., Fast, P., Lumme, K., & Peltoniemi, J. (1996). Light scattering by gaussian random particles: Ray optics approximation. *Journal of Quantitative Spectroscopy & Radiative Transfer*, *55*(5), 577–601.(Light Scattering by Non-Spherical Particles). https://doi.org/10.1016/0022-4073(96)00003-9

Murayama, T. H., Okamoto, H., Kaneyasu, N., Kamataki, H., & Miura, K. (1999). Application of lidar depolarization measurement in the atmospheric boundary layer: Effects of dust and sea-salt particles. *Journal of Geophysical Research*, *104*(D24), 31781–31792. https://doi.org/10.1029/1999JD900503

Murphy, D. M., Anderson, J. R., Quinn, P. K., McInnes, L. M., Brechtel, F. J., Kreidenweis, S. M., et al. (1998). Influence of sea-salt on aerosol radiative properties in the Southern Ocean marine boundary layer. *Nature*, *392*(6671), 62–65. https://doi.org/10.1038/32138

Nousiainen, T., & Kandler, K. (2015). Light scattering by atmospheric mineral dust particles. In A. A. Kokhanovsky (Ed.), *Light scattering reviews 9: Light scattering and radiative transfer* (pp. 3–52). Berlin, Heidelberg: Springer Berlin Heidelberg. https://doi.org/10.1007/978-3-642-37985-7_1

Patterson, J. P., Collins, D. B., Michaud, J. M., Axson, J. L., Sultana, C. M., Moser, T., et al. (2016). Sea spray aerosol structure and composition using cryogenic transmission electron microscopy. *ACS Central Science*, *272*(1), 40–47. https://doi.org/10.1021/acscentsci.5b00344

Peart, A., & Evans, J. R. G. (2011). Study of sea salt particles launched by bubble burst. *Bubble Science, Engineering and Technology*, *3*(2), 64–72. https://doi.org/10.1179/1758897911Y.0000000004

Penttilä, A., Zubko, E., Lumme, K., Muinonen, K., Yurkin, M. A., Draine, B., et al. (2007). Comparison between discrete dipole implementations and exact techniques. *Journal of Quantitative Spectroscopy & Radiative Transfer*, *106*(1), 417–436.(IX Conference on Electromagnetic and Light Scattering by Non-Spherical Particles). https://doi.org/10.1016/j.jqsrt.2007.01.026

Porter, J. N., & Clarke, A. D. (1997). Aerosol size distribution models based on in situ measurements. *Journal of Geophysical Research*, *109*, 6035–6045.

Pósfai, M., Anderson, J. R., Buseck, P. R., & Sievering, H. (1995). Compositional variations of sea-salt-mode aerosol particles from the north atlantic. *Journal of Geophysical Research*, *100*(D11), 23063–23074. https://doi.org/10.1029/95JD01636

Sakai, T., Nagai, T., Mano, Y., Zaizen, Y., & Inomata, Y. (2012). Aerosol optical and microphysical properties as derived from collocated measurements using polarization lidar and direct sampling. *Atmospheric Environment*, *60*, 419–427. https://doi.org/10.1016/j.atmosenv.2012.06.068

Sakai, T., Nagai, T., Zaizen, Y., & Mano, Y. (2010). Backscattering linear depolarization ratio measurements of mineral, sea-salt, and ammonium sulfate particles simulated in a laboratory chamber. *Applied Optics*, *49*(23), 4441–4449. https://doi.org/10.1364/AO.49.004441

Sakai, T., Shibata, T., Kwon, S.-A., Kim, Y.-S., Tamura, K., & Iwasaka, Y. (2000). Free tropospheric aerosol backscatter, depolarization ratio, and relative humidity measured with the raman lidar at nagoya in 1994–1997: Contributions of aerosols from the asian continent and the Pacific Ocean. *Atmospheric Environment*, *34*(3), 431–442. https://doi.org/10.1016/S1352-2310(99)00328-3

Sayer, A. M., Smirnov, A., Hsu, N. C., & Holben, B. N. (2012). A pure marine aerosol model, for use in remote sensing applications. *Journal of Geophysical Research*, *117*, D05213. https://doi.org/10.1029/2011JD016689

Schulz, F. M., Stamnes, K., & Stamnes, J. J. (1999). Point group symmetries in electromagnetic scattering. *Journal of the Optical Society of America. A*, *16*, 853–865.

Shettle, E. P., & Fenn, R. W. (1979). Models for the aerosols of the lower atmosphere and the effects of humidity variations on their optical properties (AFGL Technical Report No. AFGL-TR-79–021A). *Air Force Geophysics Laboratory*. Retrieved from https://apps.dtic.mil/docs/citations/ADA08595

Sun, B., Bi, L., Yang, P., Kahnert, M., & Kattawar, G. (2019). *Invariant imbedding t-matrix method for light scattering by nonspherical and inhomogeneous particles*. Amsterdam: Elsevier.

Tang, I. N., Tridico, A. C., & Fung, K. H. (1997). Thermodynamic and optical properties of sea salt aerosols. *Journal of Geophysical Research: Atmosphere*, *102*(D19), 23269–23275. https://doi.org/10.1029/97JD01806

Torge, A., Macke, A., Heinold, B., & Wauer, J. (2011). Solar radiative transfer simulations in Saharan dust plumes: Particle shapes and 3-d effect. *Tellus B*, *63*(4), 770–780. https://doi.org/10.1111/j.1600-0889.2011.00560.x

Ueda, S., Hirose, Y., Miura, K., & Okochi, H. (2014). Individual aerosol particles in and below clouds along a mt. fuji slope: Modification of sea-salt-containing particles by in-cloud processing. *Atmospheric Research*, *137*, 216–227. https://doi.org/10.1016/j.atmosres.2013.10.011

Virtanen, P., Gommers, R., Oliphant, T. E., Haberland, M., Reddy, T., & Cournapeau, D., et al. (2020). Scipy 1.0: Fundamental algorithms for scientific computing in python. *Nature Methods*, *17*(3), 261–272. https://doi.org/10.1038/s41592-019-0686-2

Wandinger, U. (2005). Raman lidar. In C. Weitkamp (Ed.), *Lidar: Range-resolved optical remote sensing of the atmosphere* (pp. 241–271). New York, NY: Springer. https://doi.org/10.1007/0-387-25101-4_9

Wang, Z., Bi, L., Yi, B., & Zhang, X. (2019). How the inhomogeneity of wet sea salt aerosols affects direct radiative forcing. *Geophysical Research Letters*, *46*(3), 1805–1813. https://doi.org/10.1029/2018GL081193

Wells, N. C. (2011). *The atmosphere and ocean: A physical introduction* (3rd ed.) John Wiley & Sons, Inc.

Wise, M. E., Biskos, G., Martin, S. T., Russell, L. M., & Buseck, P. R. (2005). Phase transitions of single salt particles studied using a transmission electron microscope with an environmental cell. *Aerosol Science & Technology*, *39*(9), 849–856. https://doi.org/10.1080/02786820500295263

Wriedt, T. (2002). Using the t-matrix method for light scattering computations by non-axisymmetric particles: Superellipsoids and realistically shaped particles. *Particle & Particle Systems Characterization*, *19*(4), 256–268. https://doi.org/10.1002/1521-4117(200208)19:4⟨256::AID-PPSC256⟩3.0.CO;2-8

Yin, Z., Ansmann, A., Baars, H., Seifert, P., Engelmann, R., Radenz, M., et al. (2019). Aerosol measurements with a shipborne sun–sky–lunar photometer and collocated multiwavelength raman polarization lidar over the atlantic ocean. *Atmospheric Measurement Techniques*, *12*(10), 5685–5698. https://doi.org/10.5194/amt-12-5685-2019

Yurkin, M. A., & Hoekstra, A. G. (2007). The discrete dipole approximation: An overview and recent developments. *Journal of Quantitative Spectroscopy & Radiative Transfer*, *106*(1), 558–589.(IX Conference on Electromagnetic and Light Scattering by Non-Spherical Particles). Retrieved from https://doi.org/10.1016/j.jqsrt.2007.01.034

Yurkin, M. A., & Hoekstra, A. G. (2011). The discrete-dipole-approximation code adda: Capabilities and known limitations. *Journal of Quantitative Spectroscopy & Radiative Transfer*, *112*(13), 2234–2247. https://doi.org/10.1016/j.jqsrt.2011.01.031

Yurkin, M. A., & Hoekstra, A. (2014). *User manual for the discrete dipole approximation code adda 1.3b4*. Retrieved from https://github.com/adda-team/adda/releases/tag/v1.3b4

Yurkin, M. A., & Kahnert, M. (2013). Light scattering by a cube: Accuracy limits of the discrete dipole approximation and the T-matrix method. *Journal of Quantitative Spectroscopy & Radiative Transfer*, *123*, 176–183.

Yurkin, M. A., Maltsev, V. P., & Hoekstra, A. G. (2006). Convergence of the discrete dipole approximation. ii. an extrapolation technique to increase the accuracy. *Journal of the Optical Society of America. A*, *23*(10), 2592–2601. https://doi.org/10.1364/JOSAA.23.002592

Zeng, J., Zhang, G., Long, S., Liu, K., Cao, L., Bao, L., & Li, Y. (2013). Sea salt deliquescence and crystallization in atmosphere: An in situ investigation using x-ray phase contrast imaging. *Surface and Interface Analysis*, *45*(5), 930–936. https://doi.org/10.1002/sia.5184

Zieger, P., Väisänen, O., Corbin, J. C., Partridge, D. G., Bastelberger, S., Mousavi-Fard, M., et al. (2017). Revising the hygroscopicity of inorganic sea salt particles. *Nature Communications*, *8*(1), 15883. https://doi.org/10.1038/ncomms15883